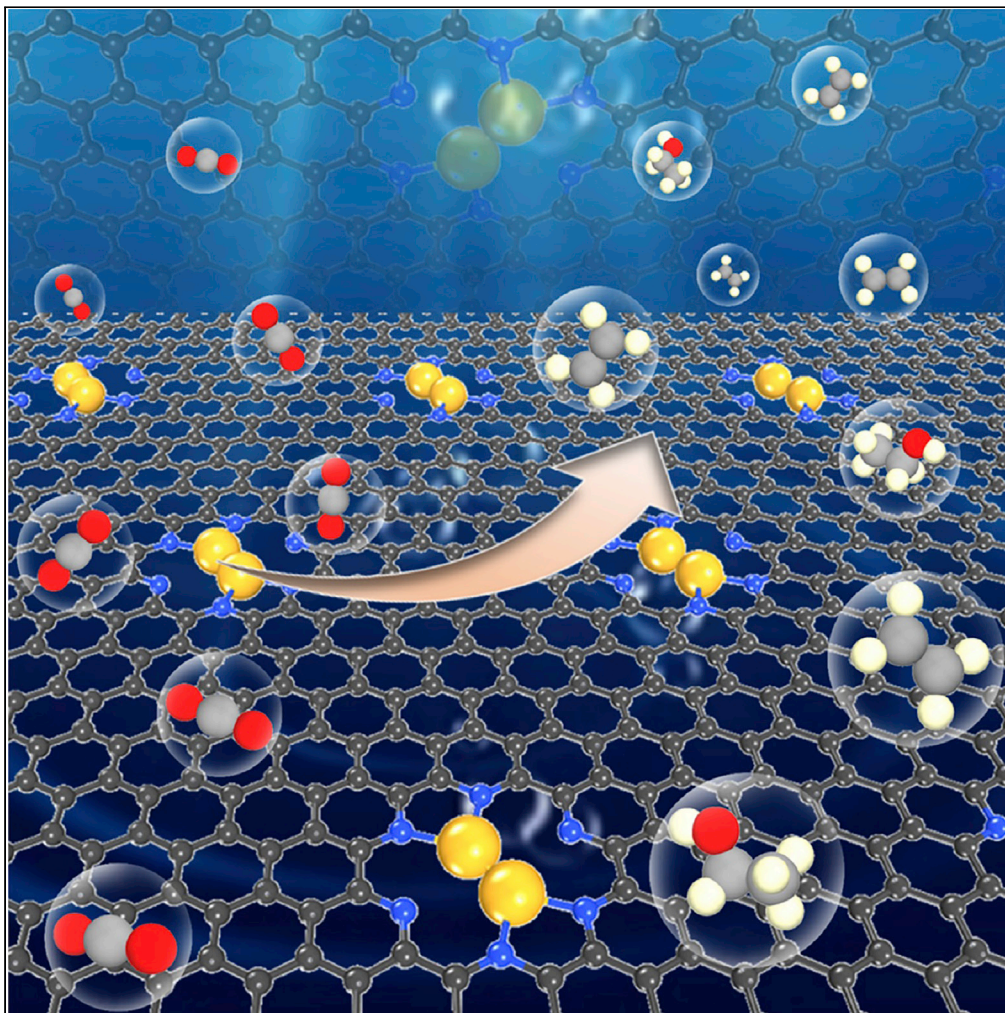


Article

Selective C–C Coupling by Spatially Confined Dimeric Metal Centers



Yanyan Zhao, Si Zhou, Jijun Zhao

sizhou@dlut.edu.cn

HIGHLIGHTS

Dual metal centers provide an exclusive pathway for CO₂ reduction to C₂ products

Activity and selectivity are modulatable by the metal-support interaction

Fe₂ dimer anchored on C₂N leads to remarkable selectivity for ethanol

Zhao et al., iScience 23, 101051
May 22, 2020 © 2020 The Author(s).
<https://doi.org/10.1016/j.isci.2020.101051>



Article

Selective C–C Coupling by Spatially Confined Dimeric Metal Centers

Yanyan Zhao,¹ Si Zhou,^{1,2,*} and Jijun Zhao¹

SUMMARY

Direct conversion of carbon dioxide (CO_2) to high-energy fuels and high-value chemicals is a fascinating sustainable strategy. For most of the current electrocatalysts for CO_2 reduction, however, multi-carbon products are inhibited by large overpotentials and low selectivity. Herein, we exploit dispersed 3d transition metal dimers as spatially confined dual reaction centers for selective reduction of CO_2 to liquid fuels. Various nitrogenated holey carbon monolayers are shown to be promising templates to stabilize these metal dimers and dictate their electronic structures, allowing precise control of the catalytic activity and product selectivity. By comprehensive first-principles calculations, we screen the suitable transition metal dimers that universally have high activity for ethanol ($\text{C}_2\text{H}_5\text{OH}$). Furthermore, remarkable selectivity for $\text{C}_2\text{H}_5\text{OH}$ against other C_1 and C_2 products is found for Fe_2 dimer anchored on C_2N monolayer. The role of electronic coupling between the metal dimer and the carbon substrates is thoroughly elucidated.

INTRODUCTION

Production of liquid fuels by catalytic conversion of CO_2 , the main greenhouse gas and meanwhile an abundant carbon feedstock, has been regarded as an appealing strategy to solve both energy and environmental crises, albeit facing great challenges (Birdja et al., 2019; Jia et al., 2019; Amal et al., 2017). Copper-based materials have been widely adopted as catalysts for electro-reduction of CO_2 to multi-carbon (C_2 or C_{2+}) products (Zheng et al., 2019). Although fairly good activity can be achieved by modification or morphology engineering of copper, such as sculpturing it into nanoparticles or nanocubes, doping or alloying, and making oxide-derived copper, the selectivity and efficiency of most copper-based electrocatalysts remain unsatisfactory for commercialization of the CO_2 conversion technique to high-energy fuels and high-value chemicals (Gao et al., 2019; Kim et al., 2017; Wang et al., 2018; Zhou et al., 2018).

Recently, transition metal atoms dispersed on nitrogen-doped porous carbon nanomaterials emerge as a promising category of electrocatalysts for CO_2 reduction, which have maximum atomic efficiency, high electrical conductivity and good durability, and can be facilely synthesized in the laboratory (Bayatsar-madi et al., 2017; Chen et al., 2019; Cheng et al., 2018; Wang et al., 2019). The transition metal atoms are usually anchored in the pores of the carbon matrix and coordinated with the nitrogen atoms, exhibiting unique electronic states and acting as isolated reaction centers for CO_2 reduction. Remarkable activity and selectivity toward carbon monoxide (CO) has been observed for various dispersed transition metal atoms (Fe, Co, Ni, Mn, and Cu) on N-doped graphene, carbon nanosheets or nanospheres, with selectivity up to 97% and Faradaic efficiency above 80% (Jiang et al., 2018; Ren and Zhao, 2020; Wang et al., 2019; Yang et al., 2018; Zhang et al., 2018). First-principle calculations show that the activity highly depends on the type of metal atoms, which provide different binding strengths with the reaction intermediates (Ju et al., 2017). The single metal sites also have an advantage of suppressing the competing hydrogen evolution reaction (HER), due to the unique adsorption configuration of H^* species compared with those on the transition metal surfaces (Bagger et al., 2017).

Furthermore, homonuclear and heteronuclear dimers of transition metal immobilized in carbon-based nanostructures, such as Fe_2 and Fe-Co on nitrogenated graphitic carbon materials, Fe-Ni on N-doped graphene, and Pt-Ru on g- C_3N_4 , have been synthesized in the laboratory (Wang et al., 2017, 2018; Ye et al., 2019; Zhou et al., 2019). This opens up the windows for a broader range of chemical processes that require dual reaction centers either with enhanced activity or carrying different functionalities simultaneously. For

¹Key Laboratory of Materials Modification by Laser, Ion and Electron Beams (Dalian University of Technology), Ministry of Education, Dalian 116024, China

²Lead Contact

*Correspondence:
sizhou@dlut.edu.cn

<https://doi.org/10.1016/j.isci.2020.101051>



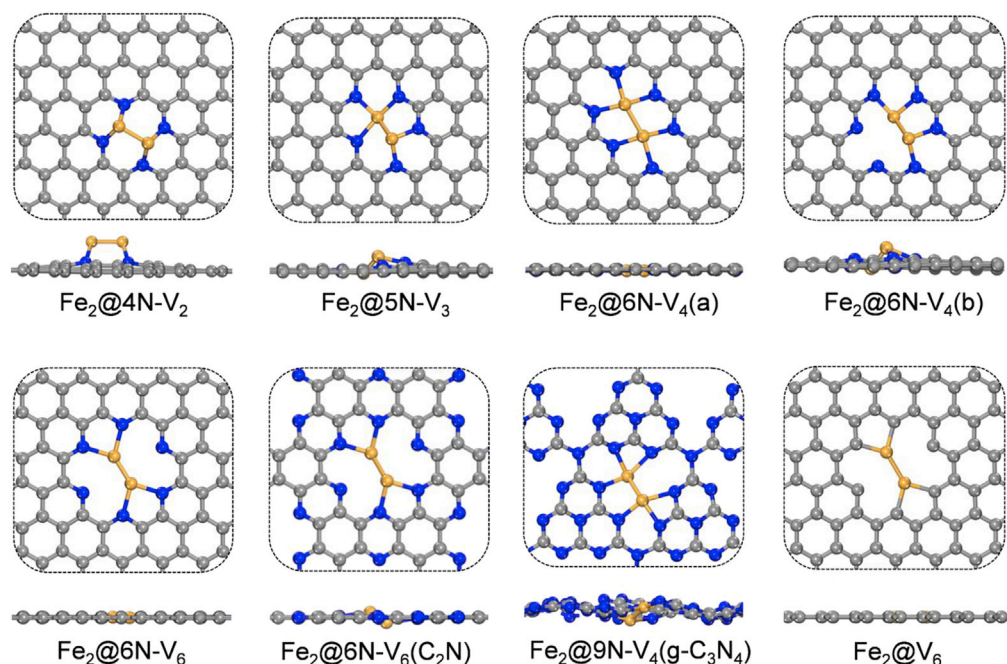


Figure 1. Atomic Structures of a Fe_2 Dimer Anchored on Various Nitrogenated Holey Carbon Monolayers (Top Panel: Top View; Bottom Panel: Side View)

The C, N, and Fe atoms are shown in gray, blue, and orange colors, respectively.

instance, Ren et al. fabricated diatomic Fe-Ni sites embedded in nitrogenated carbon (Ren et al., 2019). By taking advantage of the strong binding capability of Fe with CO_2 molecule and the weak adsorption of CO on Ni, they achieved impressively high selectivity of 99% for CO and Faradaic efficiency above 90% over a wide potential range from -0.5 to -0.9 V, reaching 98% at -0.7 V versus reversible hydrogen electrode (RHE). On the theoretical side, a Cu_2 dimer supported on the C_2N monolayer was predicted to have high selectivity for methane (CH_4), whereas dimerization of two CO species leading to the formation of ethene (C_2H_4) is possible with an energy cost of 0.76 eV (Zhao et al., 2018). Heteronuclear dimers such as V-Mo on 2D C_2N and Cu-B on g- C_3N_4 have been shown to effectively reduce CO_2 to ethanol ($\text{C}_2\text{H}_5\text{OH}$) and C_2H_4 , owing to the synergistic interaction and asymmetric coupling between two reaction centers yielding favorable binding strength for the formation of C_2 intermediates (Li et al., 2019; He et al., 2020).

Two adjacent metal atoms that are spatially confined in a hole of N-doped carbon materials as unique active sites not only enable the simultaneous fixation of two CO_2 molecules but also sterically limit the reaction pathways that may be beneficial for C–C coupling toward C_2 or C_{2+} products. Moreover, various combinations of metal dimers and carbon substrates give high degrees of freedom for modulating the catalytic performance. However, the atomistic mechanism and composition recipe of such heterogeneous catalysts remain largely unknown, which impede their rational design and experimental synthesis for practical uses.

Here we exploit 3d transition metal dimers immobilized on various nitrogenated holey carbon sheets for selective reduction of CO_2 to C_2 products. By systematic first-principle calculations, the detailed C–C coupling mechanism on the spatially confined dual metal centers has been elucidated for the first time. The suitable transition metal elements and carbon substrates that lead to high activity and selectivity for $\text{C}_2\text{H}_5\text{OH}$ and C_2H_4 are screened, and the underlying electronic structure-activity relationship is unveiled. These theoretical explorations illuminate important clues for precisely engineering the dispersed metal catalysts on porous carbon nanomaterials for direct conversion of greenhouse gas to multi-carbon hydrocarbons and oxygenates.

Substrate	E_{form} (eV/Å)	E_b (eV)	d (Å)		CT (e)	$\Delta E_{\text{CO}_2^*}$ (eV)
			Fe–Fe	N–Fe		
4N-V ₂	0.17	−5.01	2.09	1.98	0.71	−1.02
5N-V ₃	0.19	−7.33	1.91	1.87	0.97	−1.15
6N-V ₄ (a)	0.20	−9.47	2.21	1.94	0.96	−0.11
6N-V ₄ (b)	0.21	−7.48	2.14	1.98	0.81	−1.15
6N-V ₆	0.16	−6.02	1.96	2.00	0.76	−1.12
C ₂ N	−	−5.80	2.01	1.97	0.74	−0.64
g-C ₃ N ₄	−	−5.09	1.98	1.99	0.72	−1.58
V ₆	0.67	−12.03	2.21	1.94	0.87	−0.30

Table 1. Structural and Energetic Properties of Supported Fe₂ Dimer

Formation energy (E_{form}) of various nitrogenated 2D holey carbon materials, binding energy (E_b) of a Fe₂ dimer on the carbon sheet, bond length (d) of Fe–Fe and N–Fe/C–Fe bonds, Mulliken charge transfer (CT) from Fe₂ to the carbon sheet, and adsorption energy of a CO₂ molecule ($\Delta E_{\text{CO}_2^*}$) on the supported Fe₂ dimer.

RESULTS AND DISCUSSION

In the laboratory, N-doped graphitic carbon materials with controllable doping contents (up to 16.7% of N content) and atomic geometries can be achieved via either direct synthesis or posttreatment (Xue et al., 2012; Xu et al., 2018; Qu et al., 2010). Here we focused on pyridine N dopants in graphene, which are the main doping species at high N contents and are usually associated with the vacancies or pores of the carbon basal plane (Sheng et al., 2011; Sarau et al., 2017). As displayed in Figure 1, we considered a series of N-doped holey graphene monolayers, comprising C vacancies of various sizes (denoted as V_n, $n = 2, 3, 4, 6$) with the edges coordinated with different numbers of N atoms (denoted as mN, $m = 4, 5, 6$). Specifically, 4N-V₂, 5N-V₃, and 6N-V₄ systems can be viewed as four, five, and six N atoms decorating the edges of di-vacancy, tri-vacancy, and tetra-vacancy in graphene, respectively, all of which have been commonly observed in experiment (He et al., 2014; Lin et al., 2015; Wang et al., 2018). Note that the V₆ pore in graphene is a favorable defect according to transmission electron microscopy experiment (Robertson et al., 2015), and our previous calculation showed that N-doped V₆ (namely 6N-V₆) has extraordinary thermodynamic stability (Luo et al., 2013). We further created a number of randomly N-doped graphene lattices, which shows that the 6N-V₆ configuration would emerge as N doping content reaches 10% (see Figure S1 for details). Besides the N-doped graphitic sheets, we also considered the synthetic carbon nitride monolayers, including g-C₃N₄ and C₂N (Zhao et al., 2014; Mahmood et al., 2015). All these porous N-coordinated carbon sheets have formation energies (defined by Equation S1 in Supplemental Information) in the range of 0.16–0.21 eV/Å, whereas the N-free V₆ is higher in energy by over 0.46 eV/Å than the others (Table 1). These nitrogenated 2D holey carbon materials are ideal templates to stabilize and disperse metal atoms or small clusters. Indeed, isolated Fe₂, Fe-Ni, and Fe-Co dimers embedded in 6N-V₄(a), as well as Fe₂ and Pt-Ru dimers anchored on g-C₃N₄ have already been realized in experiment (Ye et al., 2019; Wang et al., 2017; Zhou et al., 2019; Ren et al., 2019; Tian et al., 2018).

To evaluate the capability of various supported metal dimers for CO₂ reduction toward C₂ products, we first explored the atomic structures, electronic and adsorption properties of dimeric 3d transition metal clusters on the 6N-V₆ monolayer (as will be shown later, this substrate gives metal dimers the highest activity for CO₂ reduction). As presented in Figures 1 and S2, all metal dimers are embedded in the hole of the graphitic sheet, except that Sc₂ with a larger atomic size induces a noticeable buckling of 0.94 Å in the out-of-plane direction. Four N–metal bonds are formed with bond length of 1.95–2.09 Å, and the metal–metal bond length ranges from 1.96 Å to 2.79 Å (Table 2). The binding energy (defined by Equation S2 in Supplemental Information) between the metal dimer and the graphitic sheet is −4.29 to −10.28 eV, excluding the possibility of dissociation or aggregation of the metal dimer. The thermal stability of these carbon-substrate-anchored metal dimers was further assessed by *ab initio* molecular dynamics (AIMD) simulations, which manifest that they can sustain at least 800 K for 10 ps with small vertical displacement of metal atoms (<0.2 Å) (see Figure S3 for details), suggesting superior thermal stability for practical uses.

Metal Dimer	E_b (eV)	d (Å)		ΔE (eV)		ϵ_d (eV)
		M–M	N–M	CO_2	2CO_2	
Sc_2	−10.28	2.79	2.09	−3.40	−3.71	1.16
Ti_2	−8.50	2.17	1.99	−2.85	−3.31	0.62
V_2	−8.80	2.14	1.96	−2.26	−	0.41
Cr_2	−4.99	2.16	1.97	−1.44	−0.76	0.07
Mn_2	−6.52	2.04	2.01	−1.05	−0.48	−0.42
Fe_2	−6.02	1.96	2.00	−1.12	−0.50	−1.00
Co_2	−5.71	2.10	1.95	−1.20	−	−1.09
Ni_2	−5.93	2.17	2.00	−0.82	−	−1.12
Cu_2	−4.29	2.35	1.96	−0.35	−	−2.08

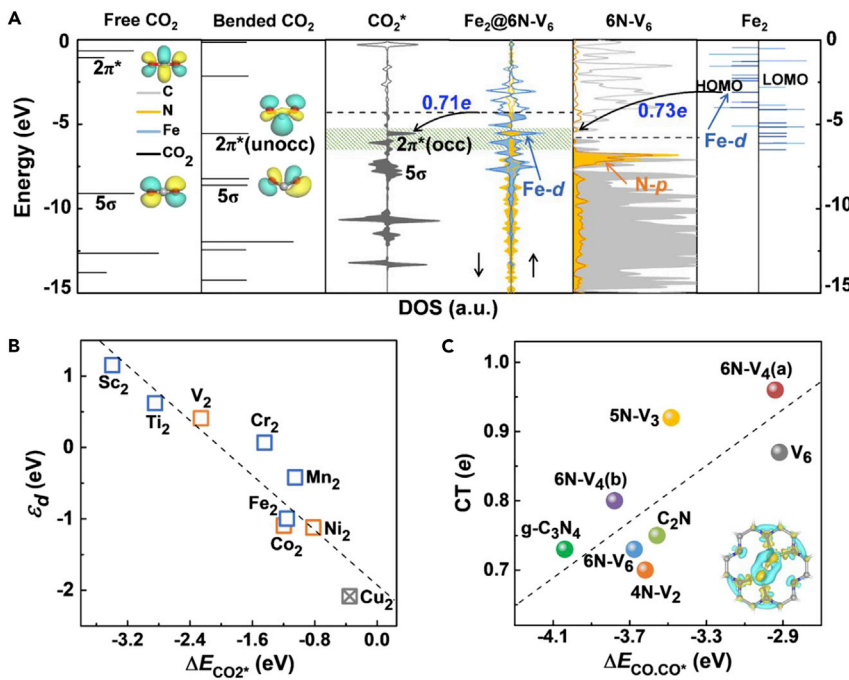
Table 2. Structural and Energetic Properties of Various Supported 3d Transition Metal Dimers

Binding energy (E_b) of various 3d transition metal dimers anchored on the 6N-V₆ monolayer, bond lengths (d) of metal dimer (M–M) and N–metal (N–M), adsorption energy of single and dual CO₂ molecules on the supported metal dimers (ΔE), and the d band center (ϵ_d) of the supported metal dimers (Hammer and Nørskov, 2000).

A CO₂ molecule can favorably chemisorb on these dispersed metal dimers except Cu₂. The molecule is bonded in the bidentate configuration with O–C–O angle of 124.90–141.96°. The C atom and one of the O atoms of CO₂ form two bonds with the underlying metal atoms; the C–O bond length is elongated to 1.21–1.36 Å, compared with 1.16 Å for a free CO₂ molecule. The dynamic process of CO₂ adsorption was also examined by AIMD simulations at 100 K and 300 K, respectively, both showing that the molecule can quickly chemisorb on the dimeric metal centers within a simulation time of 1 ps (see Videos S1 and S2 for the dynamic movies). The adsorption energy (defined by Equation S3 in Supplemental Information) of CO₂ ranges from −0.82 eV to −3.40 eV. Overall speaking, stronger binding is provided by the metal element with fewer d electrons. The trend of activity can be understood by the electronic density of states (DOS) shown in Figure 2A. Taking Fe₂@6N-V₆ as an example, hybridization between the d orbitals of Fe₂ dimer and the p orbitals of 6N-V₆ monolayer substrate is evident, with prominent electronic states close to the Fermi level mainly contributed by the Fe atoms (see Figure S4 for projected DOS). Electron transfer of 0.73 e occurs from Fe₂ to 6N-V₆ monolayer, which lifts the Fermi level of the hybrid system above the $2\pi^*$ state of CO₂. As a result, Fe₂@6N-V₆ can favorably donate about 0.71 electrons to the antibonding orbital of CO₂, as manifested by the differential charge densities in Figure 3A, which is a general mechanism for activation of reactant molecules on metal active centers (Liu et al., 2018). As depicted in Figure 2B, CO₂ adsorption energy generally follows a linear relationship with the d band center of the supported metal dimers (relative to the Fermi level), as the metal dimer with a higher d band center would provide stronger binding with CO₂ (Hammer and Nørskov, 2000).

In addition, we examined the capability of various dispersed 3d transition metal dimers for activating two CO₂ molecules simultaneously, which is a prerequisite for C–C coupling to yield C₂ products. Several candidate systems including Sc₂, Ti₂, Cr₂, Mn₂, and Fe₂ dimers on the 6N-V₆ monolayer have adsorption energies of −3.71 to −0.48 eV for fixation of two CO₂ molecules (Figures 3 and S5), whereas the other metal dimers are only able to bind one CO₂ molecule. Considering that Fe is an earth-abundant element and dispersed Fe atoms and dimers can be readily obtained in the experiment (Ye et al., 2019; Tian et al., 2018), thereafter we explored Fe₂ dimer on various nitrogenated 2D holey carbon materials as a representative of dual metal centers.

Figure 1 presents the structures of a Fe₂ dimer immobilized on several 2D carbon substrates. The dimer forms 4–6 bonds with the neighboring N or C atoms, having bond lengths of 1.91–2.21 Å for Fe–Fe and 1.87–2.00 Å for N–Fe (C–Fe) bonds, respectively, and the binding energies are −5.01 to −12.03 eV (Table 1). The Fe₂ dimer exhibits different buckling height in the out-of-plane direction (0.01–2.06 Å) and meanwhile induces some local vertical distortions on the carbon basal plane (0.09–0.35 Å). The dimer-substrate coupling strength depends on the size of the hole as well as the saturation degree of the edge atoms. For

**Figure 2. Electronic Structure-Activity Relationship**

(A) From left to right: molecular orbital levels or local density of states (DOS) of a free and a bended (with C–O–C angle of 130°) CO₂ molecule in vacuum, an adsorbed CO₂ molecule on Fe₂@6N-V₆, an individual 6N-V₆ monolayer, and a Fe₂ dimer. The insets display the HOMO and LUMO charge densities of CO₂. The energy is relative to the vacuum. The dashed line shows the Fermi level, with the occupied states shadowed. The hybridization region between *d* orbital of Fe atoms and 2π* state of CO₂ is shadowed in green. The dark blue and orange colors represent the *d* orbital of Fe atoms and *p* orbital of N atoms, respectively.

(B) The *d* band center (ϵ_d) of various supported 3*d* transition metal dimers as a function of the adsorption energy of single CO₂ molecule. The blue/orange/gray symbols denote that two/one/none CO₂ molecule can be chemisorbed on the metal dimer. The dashed line is a linear fit of the data points.

(C) Charge transfer (CT) from the Fe₂ dimer to various nitrogenated carbon holey monolayer as a function of the adsorption energy of dual CO molecules. The dashed line is a linear fit of the data points. The insert shows the differential charge density of Fe₂@6N-V₆. The yellow and cyan colors represent the electron accumulation and depletion regions, respectively, with an isosurface value of 0.005 e/Å³.

instance, binding strength between Fe₂ and 4N-V₂, 5N-V₃, and 6N-V₄(a) increases with both N content and hole size. The bonding interaction between Fe₂ and g-C₃N₄ or C₂N is relatively weak, due to the electronic saturation of these two semiconducting carbon nitride monolayers (as manifested by their large band gaps). In sharp contrast, Fe₂ is strongly anchored on the nitrogen-free V₆ defect that has six unsaturated carbon atoms on the hole edge, thereby leading to the largest binding energy of -12.03 eV.

All the supported Fe₂ dimers are able to chemisorb two CO₂ molecules with total adsorption energies of -0.23 to -1.62 eV (compared with -0.11 to -1.58 eV for adsorption of single CO₂ molecule), as revealed by Figure 3B. Our nudged elastic band (NEB) calculations show that adsorption of the second CO₂ molecule involves kinetic barriers of 0.29–1.04 eV. Both CO₂ molecules are bended with O–C–O angle of 141.00–152.13° and elongated C–O bond lengths of 1.17–1.29 Å. The C atom in each CO₂ is bonded to the underlying Fe atom with Fe–C bond length of 1.93–2.12 Å. Furthermore, we investigated the interaction between the dispersed Fe₂ dimers and the CO molecule, which is an important reaction intermediate in the CO₂ reduction process. Our calculations indicate strong binding of CO on the anchored Fe₂ dimers, with adsorption energies of -2.94 to -4.04 eV (-1.94 to -2.70 eV) for two (one) CO molecules. Consequently, desorption of CO from dual metal centers would be rather difficult, which allows further protonation of CO and thus provides the opportunity for successive C–C coupling.

The distinct binding capability of various supported Fe₂ dimers with gas molecules can be related to the electronic coupling between Fe₂ and the carbon substrate. As displayed in Figure 2C, the amount of charge

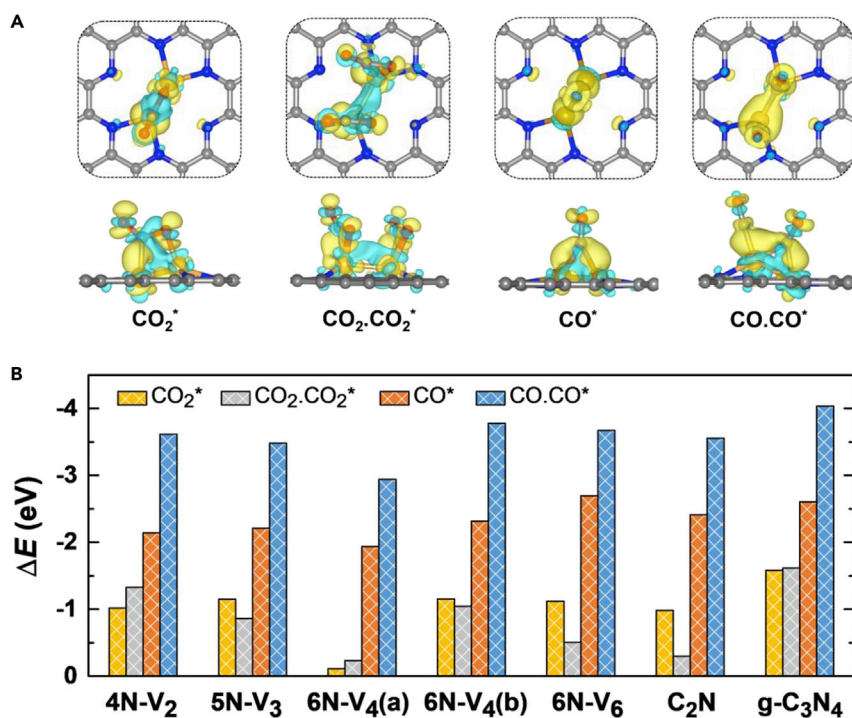


Figure 3. Structures and Energies of Molecular Adsorption

(A) From left to right: differential charge densities of single and dual CO_2 molecules, single and dual CO molecules adsorbed on $\text{Fe}_2@6\text{N-V}_6$. The yellow and cyan colors represent the electron accumulation and depletion regions, respectively, with an isosurface value of $0.005 \text{ e}/\text{\AA}^3$.

(B) Adsorption energies of single and dual CO_2 and CO molecules on the Fe_2 dimer anchored on various nitrogenated holey carbon monolayers. The C, N, O, and Fe atoms are shown in gray, blue, red, and orange colors, respectively.

transfer from Fe_2 to the substrate varies from 0.71 e to 0.97 e. Generally speaking, less electron transfer leads to higher activity of the Fe_2 dimer for CO_2 and CO chemisorption, which is consistent with the trend of binding energies between Fe_2 and the carbon templates discussed before (Table 1). It is the N content, the degree of electronic saturation of the hole edge, and the bond configuration of Fe_2 in the hole that jointly determine the coupling strength between the metal dimer and the carbon sheets. Therefore, the nitrogenated 2D holey carbon materials with diverse morphologies and controllable N contents can not only stabilize and disperse metal dimers but also dictate the electronic structures and activity of the anchored metal dimers. By choosing proper metal elements and substrates, it is possible to delicately mediate their coupling strength and charge transfer, endowing large degree of freedom to optimize the activity and selectivity of various supported metal dimers for CO_2 reduction.

Note that graphitic N species are inevitably present in the experimentally synthesized N-doped carbon materials (Lin et al., 2014). To clarify their effect on the activity of the dispersed Fe_2 dimer, we investigated the CO_2 adsorption on $\text{Fe}_2@6\text{N-V}_6$ containing various numbers of graphitic N atoms at different distances from the 6N-V_6 hole (Figure S6). For all the considered systems, the CO_2 adsorption energies on the catalysts with and without substitutional N atoms on the graphene lattice differ by less than 0.16 eV, suggesting that existence of the graphitic N species has only minor impact on the catalytic properties of the Fe_2 dimer supported on pyridine holes of 2D carbon substrates.

Figure 4 shows the most efficient pathways for CO_2 reduction toward possible C_1 and C_2 products on the Fe_2 dimer immobilized on various nitrogenated carbon sheets, and the corresponding free-energy diagrams of various model systems calculated by the computational hydrogen electrode (CHE) model (Peterson et al., 2010) are given by Figures 5, S7, and S8. We used point (.) to represent the co-adsorption of two carbon intermediates on the catalyst and strigula (–) to indicate the coupling between two carbon intermediates. The maximum Gibbs free energy of formation ΔG among all the reaction steps defines the

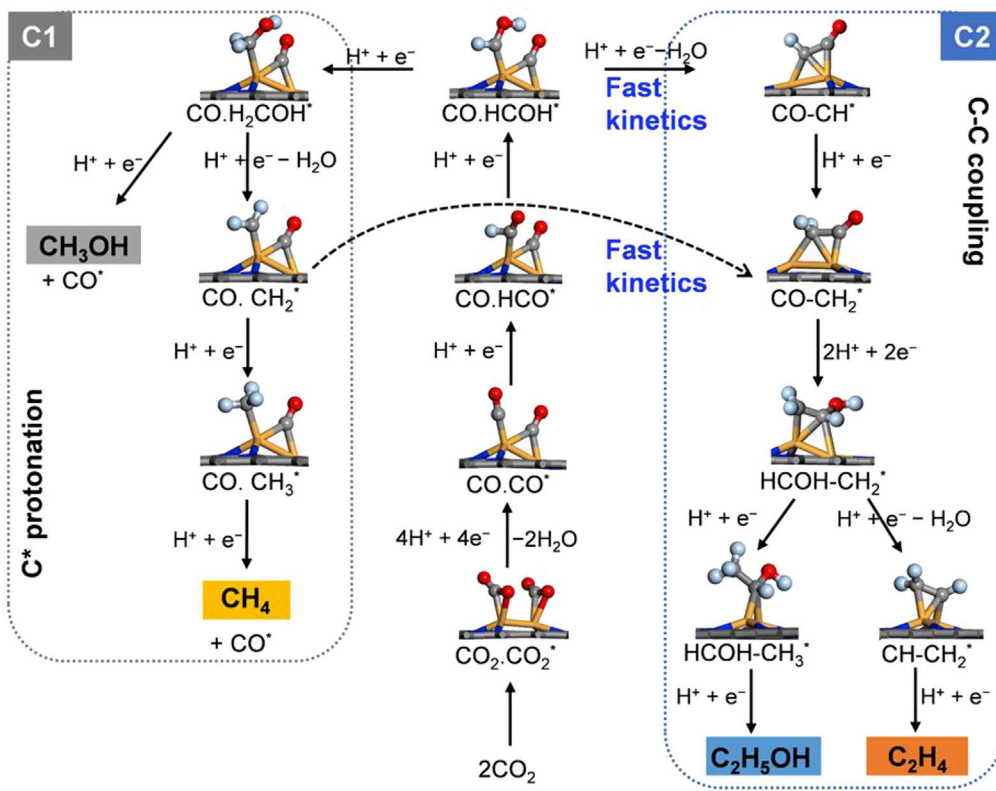


Figure 4. The CO₂ reduction pathways to various C₁ and C₂ products on the supported Fe₂ dimer
The H, C, N, O, and Fe atoms are shown in light blue, gray, blue, red, and orange colors, respectively.

rate-determining step (RDS) and is thus denoted as ΔG_{RDS} . Overall speaking, formation of C₂ products first requires the activation of dual CO₂ molecules on the catalyst. By going through the carboxyl (COOH*) pathway, two CO* intermediates can be generated; then protonation of CO* leads to C₁ products such as methanol (CH₃OH) and CH₄. Alternatively, it paves a way to the coupling between two neighboring carbon intermediates, which is energetically favorable and kinetically easy, and finally yields C₂ products (C₂H₅OH and C₂H₄). A similar path for C–C coupling was also found for the other metal dimers anchored on the nitrogenated carbon sheet, as revealed by Figure S9 for Ni₂@6N-V₆ as an example.

Specifically, formation of two CO* species on most of the considered Fe₂ dimers is uphill in the free-energy profile, involving energy steps of 0.24–0.87 eV. Then, reduction of CO* gives rise to HCO* species, which is lower in energy by up to 1.13 eV than the other possible intermediates such as COH*. (Figure S10). The CO* → HCO* conversion is endothermic with $\Delta G = 0.49$ –1.01 eV. Further protonation of HCO* leads to HCOH* and then produces a CH* species by release of a H₂O molecule. The C–C coupling reaction is most likely to occur between a CH* (or CH₂*) species and the neighboring CO*. Our NEB calculations suggest that the CO–CH* coupling is exothermic and barrierless on all the considered Fe₂ dimers, except for Fe₂@C₂N and Fe₂@C₃N₄ that involve a small kinetic barrier of about 0.22 eV (Table S1). According to previous theoretical studies (Goodpaster et al., 2016; Jiang et al., 2018), Cu(211) and (100), as the typical active surfaces for CO₂ reduction, favor dimerization of CO* or CO–HCO* coupling involving $\Delta G = -0.17$ –0.48 eV. For the present Fe₂ dimers on nitrogenated carbon sheets, however, CO–CO* or CO–HCO* coupling has higher ΔG than the values of CO–CH* by 0.84–2.42 eV and thus is unlikely to occur.

Following the C–C coupling, successive reduction of CO–CH* leads to CO–CH₂*, HCO–CH₂*, HCOH–CH₂*, HCOH–CH₃*, and finally yields C₂H₅OH. Alternatively, reduction of HCOH–CH₂* can give rise to CH–CH₂* with release of a H₂O molecule, and further protonation of CH–CH₂* eventually produces C₂H₄. These elementary reactions involve relatively small steps of 0.15–0.73 eV in free-energy profile and thus would take place readily from the thermodynamic point of view. At the last step, desorption of

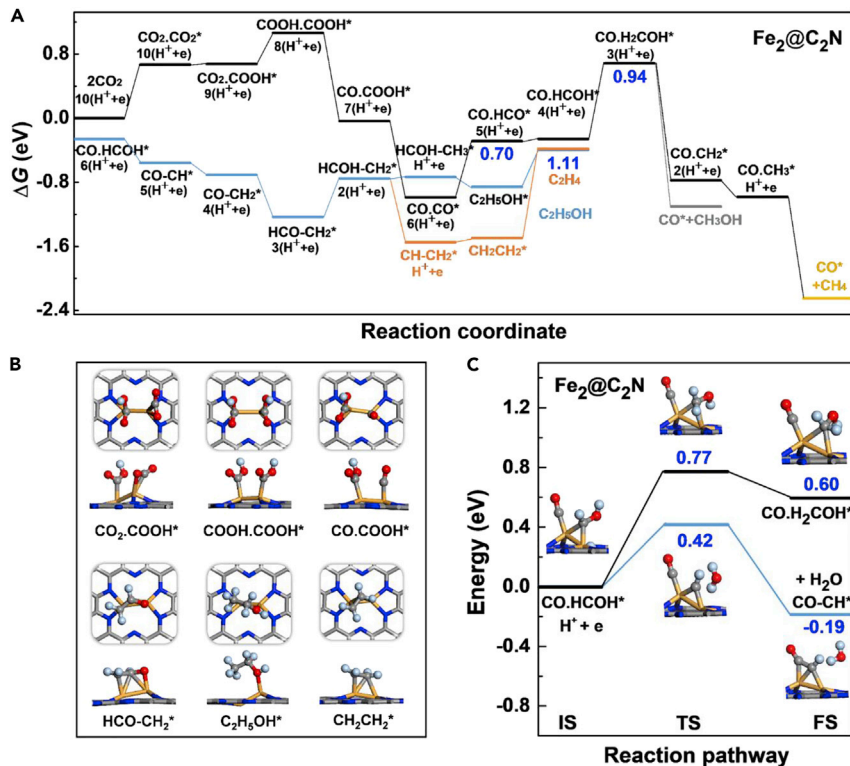


Figure 5. CO_2 Reduction Pathway

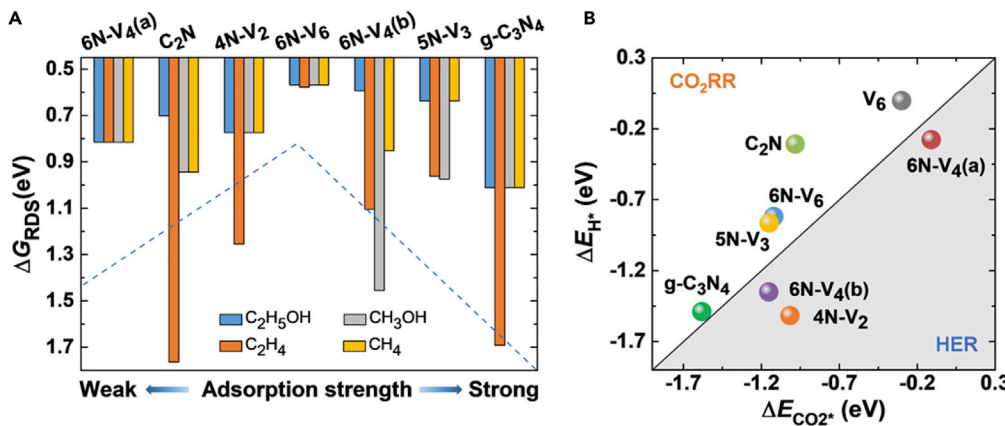
(A and B)(A) Free-energy diagram of CO_2 reduction to various C_1 and C_2 products (indicated by different colors) on $\text{Fe}_2@\text{C}_2\text{N}$. The blue numbers, from left to right, give the Gibbs free energy of formation for the rate determining step of $\text{C}_2\text{H}_5\text{OH}$, C_2H_4 , and $\text{CH}_3\text{OH}/\text{CH}_4$. The local structures of selected reaction intermediates are presented in (B). The H, C, N, O, and Fe atoms are shown in light blue, gray, blue, red, and orange colors, respectively.

(C) Competing reactions of CO,HCOH^* to form C_1 and C_2 intermediates on $\text{Fe}_2@\text{C}_2\text{N}$. The insets display the structures of initial state (IS), transition state (TS), and final state (FS). The blue numbers give the kinetic barriers (middle) and heat of reaction (right).

$\text{C}_2\text{H}_5\text{OH}^*$ and CH_2CH_2^* is endothermic by 0.11–0.59 eV and 0.23–1.69 eV, respectively. For most of the considered Fe_2 dimers, the rate-determining step for $\text{C}_2\text{H}_5\text{OH}$ production is the $\text{CO}^* \rightarrow \text{HCO}^*$ conversion. The release of C_2H_4 mainly suffers from the strong binding of CH_2CH_2^* on the catalyst, which can be overcome by the reaction heat of the corresponding reduction step (0.61–2.07 eV) (Chen et al., 2019b), as well as by adopting some strategies such as the pulse electrolysis mode to accelerate desorption of the final products (Yano et al., 2007; Qiao et al., 2014).

On the other hand, formation of C_1 products is also possible on the dispersed Fe_2 dimers. As discussed earlier, HCOH^* can be reduced to CH^* , followed by the $\text{CO}-\text{CH}^*$ coupling. Alternatively, HCOH^* may be protonated to H_2COH^* . Then, reduction of H_2COH^* yields CH_3OH or produces CH_2^* with release of a H_2O molecule followed by the generation of CH_3^* and CH_4 . For $\text{Fe}_2@4\text{N-V}_2$, $\text{Fe}_2@6\text{N-V}_6$, and $\text{Fe}_2@g-\text{C}_3\text{N}_4$, the $\text{CO}^* \rightarrow \text{HCO}^*$ conversion is the rate determining step for both C_1 products. For $\text{Fe}_2@6\text{N-V}_4(b)$ and $\text{Fe}_2@5\text{N-V}_3$, formation of CH_3OH from H_2COH^* protonation requires $\Delta G_{\text{RDS}} = 1.45$ and 0.98 eV, respectively. In particular, $\text{Fe}_2@\text{C}_2\text{N}$ encounters $\Delta G_{\text{RDS}} = 0.94$ eV and a kinetic barrier of 0.77 eV during the reaction of $\text{HCOH}^* \rightarrow \text{H}_2\text{COH}^*$ for both C_1 products, whereas the competing step of $\text{CO}-\text{HCOH}^* \rightarrow \text{CO}-\text{CH}^* + \text{H}_2\text{O}$ has much reduced $\Delta G = -0.30$ eV and a lower kinetic barrier of 0.42 eV (Figures 5A and 5C). This would lead to high selectivity for C_2 products on $\text{Fe}_2@\text{C}_2\text{N}$.

Figure 6A plots ΔG_{RDS} values for various C_1 and C_2 products from CO_2 reduction on the anchored Fe_2 dimers. Among the four products, $\text{C}_2\text{H}_5\text{OH}$ exhibits the lowest $\Delta G_{\text{RDS}} = 0.57$ –1.01 eV, and the highest activity is achieved by $\text{Fe}_2@6\text{N-V}_6$ owing to its moderate adsorption strength with the reaction intermediates (indicated by the dashed blue line in Figure 6A). Formation of C_2H_4 is less favorable with $\Delta G_{\text{RDS}} = 0.58$ –1.76 eV

**Figure 6. Catalytic Performance for CO₂ Reduction**

(A) Gibbs free energy of formation for the rate determining step (ΔG_{RDS}) for various C₁ and C₂ products from CO₂ reduction, and (B) competition between adsorption of a CO₂ molecule and an H* species on the Fe₂ dimer anchored on various nitrogenated holey carbon monolayers.

due to the strong binding of CH₂CH₂* on the Fe₂ dimers. Fe₂@6N-V₄(a), Fe₂@4N-V₂, Fe₂@6N-V₆, and Fe₂@g-C₃N₄ exhibit similar selectivity for C₂H₅OH, CH₃OH, and CH₄, whereas Fe₂@5N-V₃ favors both C₂H₅OH and CH₄ products. Remarkable selectivity for C₂H₅OH is obtained for Fe₂@C₂N and Fe₂@6N-V₄(b) with ΔG_{RDS} = 0.70 and 0.59 eV, respectively, notably lower than ΔG_{RDS} values for the other products (above 0.94 and 0.85 eV, respectively). Hence, these supported Fe₂ dimers have competitive activity but distinct selectivity with regard to the conventional Cu-based catalysts. It is known that Cu crystals mainly produce CO under low electrode potentials, whereas CH₄ and C₂H₄ are the main products at sufficiently high electrode potentials (about -1.0 V versus RHE in experiment) (Dai et al., 2017; Mistry et al., 2016). Previous calculations revealed that Cu(211) surface encounters ΔG_{RDS} = 0.74 eV for CH₄ and C₂H₄, whereas formation of CO is much more favorable with ΔG_{RDS} = 0.41 eV due to the relatively weak adsorption of CO on the Cu surface (adsorption energy ΔE = -1.01 eV) (Peterson et al., 2010). Differently, release of CO is prohibited on the present Fe₂ dimers that have strong adsorption energy of ΔE = -2.94 to -4.04 eV with CO molecule.

As the electroreduction of CO₂ usually take place in the neutral aqueous condition, we further explored the solvent effect on the catalytic behavior of supported Fe₂ dimer. As a representative, we considered an explicit solvent model of Fe₂@C₂N. Our calculations show that hydrogen bonds are formed between water molecules and some adsorbed reaction intermediates (such as CO₂, CO₂* and CO–CH*), which slightly stabilize those species on the catalyst in aqueous environment, consistent with the previous theoretical report (Zhao and Liu, 2020). The variations of CO₂ adsorption energy and Gibbs free energy of formation for elementary steps are below 0.29 eV, and the kinetic barriers of rate determining steps for various products increase by less than 0.35 eV, with regard to the model in vacuum (see Table 3 and Figure S11 for details). The predicted selectivity is consistent between the model in vacuum and in water. Therefore, free-energy calculations on electrocatalysis of CO₂ reduction using a model of catalyst in vacuum can generally predict reliable results on the trend of activity and product selectivity (De Luna et al., 2018; Zhuang et al., 2018; Li et al., 2018). Besides solvent effect, the surface charge on catalysts during the electrochemical reaction may modify the electronic states and impact the catalytic properties according to a previous theoretical report (Kim et al., 2018). Future studies with sophisticated model theory are necessary to comprehensively evaluate the catalytic performance of the proposed transition metal dimers on the nitrogenated carbon substrates.

The unique geometry and favorable adsorption properties of the Fe₂ dimers immobilized on carbon substrates bring about inimitable advantages for their catalytic behavior. First, CO, as an inevitable and even dominant product of CO₂ reduction on many metal catalysts, severely limits the formation of higher-energy-density products (Zhu et al., 2014; Sarfraz et al., 2016; Peng et al., 2018), but it would be largely suppressed on the anchored Fe₂ dimers. Second, the adjacent dual metal centers and their strong binding with CO pave an efficient pathway for C–C coupling reaction; in contrast, C–C coupling only occurs on metal

	Step	$\text{CO}_2 \rightarrow \text{CO}_2^*$	$\text{CO}_2^* + \text{CO}_2 \rightarrow \text{CO}_2\text{CO}_2^*$	$\text{CO}.\text{CH}^* \rightarrow \text{CO}-\text{CH}^*$	$\text{CO}.\text{HCOH}^* + \text{H}^+ + \text{e}^- \rightarrow$	
					$\text{CO}.\text{H}_2\text{COH}^*$	$\text{CO}-\text{CH}^* + \text{H}_2\text{O}$
Vacuum	ΔH	-0.64	0.68	0.11	0.60	-0.19
	E_a	0	0.70	0.23	0.77	0.42
Aqueous	ΔH	-0.65	0.51	-0.03	0.31	-0.18
	E_a	0	0.74	0.58	0.93	0.66

Table 3. Key Reaction Steps in Vacuum and Aqueous Condition

The reaction energy (ΔH) and kinetic barriers (E_a) for activating first and second CO_2 molecule, $\text{CO}-\text{CH}^*$ coupling, and protonation of $\text{CO}.\text{HCOH}^*$ to $\text{CO}.\text{H}_2\text{COH}^*$ species or $\text{CO}-\text{CH}^*$ with H_2O molecule in vacuum and in the aqueous condition, respectively, given in the unit of eV.

surfaces with homogenously distributed reaction sites when the coverage of CO is sufficiently high (Morales-Guio et al., 2018; Huang et al., 2017). Third, the difficult desorption of C_2H_4 from the Fe_2 dimers may result in superior selectivity for $\text{C}_2\text{H}_5\text{OH}$, which is a clean liquid fuel with high heating value. For most of the Cu based catalysts, however, the yield of $\text{C}_2\text{H}_5\text{OH}$ is quite low compared with C_2H_4 (Liang et al., 2018).

At last, we assess the activity of these supported Fe_2 dimers for HER, which is a competing reaction against CO_2 reduction and highly affects the efficiency of CO_2 conversion (Zhu et al., 2016; Cui et al., 2017). Figure 6B plots the competition between adsorption of H^* species and CO_2 molecule on the Fe_2 dimers. The H^* adsorption energy ranges from -1.52 eV to -0.28 eV. For $\text{Fe}_2@5\text{N-V}_3$, $\text{Fe}_2@6\text{N-V}_6$, $\text{Fe}_2@\text{C}_2\text{N}$, and $\text{Fe}_2@\text{C}_3\text{N}_4$, the adsorption strength of H^* species is notably weaker than that of CO_2 molecule by 0.09–0.67 eV, implying that CO_2 reduction would prevail over HER on these catalysts with either high activity or superior selectivity. For $\text{Fe}_2@4\text{N-V}_2$, $\text{Fe}_2@6\text{N-V}_4$ (a), and $\text{Fe}_2@6\text{N-V}_4$ (b), the H^* adsorption strength is stronger than that of CO_2 , which may suppress the CO_2 reduction. Combining the information in Figures 6A and 6B, we conclude that four of our considered systems are eligible for catalysis of CO_2 reduction with high activity for C–C coupling toward C_2 products. Among them, $\text{Fe}_2@\text{C}_2\text{N}$ has remarkable selectivity for ethanol; $\text{Fe}_2@5\text{N-V}_3$ favors the formation of both ethanol and methane; Fe_2 on $\text{g-C}_3\text{N}_4$ and 6N-V_6 have lower selectivity and may generate both C_1 and C_2 products. Therefore, dimeric transition metal clusters immobilized on the nitrogenated holey carbon substrates form a category of efficient electrocatalysts for reduction of CO_2 to high-value hydrocarbons and alcohols, with desired selectivity achievable by choosing proper substrate.

Conclusion

In summary, we exploited dispersed 3d transition metal dimers for CO_2 reduction to selectively produce liquid fuels. Comprehensive first-principles calculations show that nitrogenated holey carbon materials not only serve as templates to stabilize small metal clusters but also dictate their electronic structures. Specifically, controlling the metal-substrate coupling strength allows effective modulation of both activity and product selectivity. As a consequence, the spatially confined dual reaction centers within the carbon matrix exhibit the following advantageous catalytic behavior: (1) simultaneous fixation of two CO_2 molecules, (2) prohibition of CO desorption, and (3) exclusive pathway for C–C coupling with high activity. The selectivity is tunable by choosing proper substrate materials. In particular, a Fe_2 dimer embedded in the C_2N monolayer exhibits remarkable selectivity for $\text{C}_2\text{H}_5\text{OH}$ against the other C_1 and C_2 products as well as HER. These theoretical findings provide vital knowledge of the design rules of subnano metal clusters for converting greenhouse gas to high-energy fuels and high-value chemicals and meanwhile call for more experimental and theoretical efforts to advance the technologies for precise synthesis of atomically dispersed catalysts with well-controlled composition and structures.

Limitations of the Study

This study systematically exploited 3d transition metal dimers anchored on nitrogenated holey carbon monolayers for selective reduction of CO_2 to liquid fuels and screened suitable metal elements and carbon templates with high selectivity for ethanol. However, experimental realization of such superior subnano catalysts relies on the preparation of metal clusters with specific size supported on some given substrates, which may be challenging and requires the development of advanced synthesis methods.

METHODS

All methods can be found in the accompanying [Transparent Methods supplemental file](#).

SUPPLEMENTAL INFORMATION

Supplemental Information can be found online at <https://doi.org/10.1016/j.isci.2020.101051>.

ACKNOWLEDGMENTS

This work was financially supported by the National Natural Science Foundation of China (11974068, 91961204) and the Fundamental Research Funds for the Central Universities of China (DUT20LAB110). The authors acknowledge the computer resources provided by the Supercomputing Center of Dalian University of Technology.

AUTHOR CONTRIBUTIONS

S. Zhou conceived the idea; Y. Zhao carried out the calculation; S. Zhou and J. Zhao supervise the research. All authors wrote the paper.

DECLARATION OF INTERESTS

The authors declare no competing interests.

Received: January 14, 2020

Revised: March 14, 2020

Accepted: April 5, 2020

Published: May 22, 2020

REFERENCES

- Amal, R., Zhao, H., Wang, D., and Wang, L. (2017). Renewable energy conversion and storage. *Adv. Energy Mater.* 7, 1703091.
- Bagger, A., Ju, W., Varela, A.S., Strasser, P., and Rossmeisl, J. (2017). Single site porphyrine-like structures advantages over metals for selective electrochemical CO₂ reduction. *Catal. Today* 288, 74–78.
- Bayatsarmadi, B., Zheng, Y., Vasileff, A., and Qiao, S.Z. (2017). Recent advances in atomic metal doping of carbon-based nanomaterials for energy conversion. *Small* 13, 1700191.
- Birdja, Y.Y., Pérez-Gallent, E., Figueiredo, M.C., Göttle, A.J., Calle-Vallejo, F., and Koper, M.T.M. (2019). Advances and challenges in understanding the electrocatalytic conversion of carbon dioxide to fuels. *Nat. Energy* 4, 732–745.
- Chen, Y.N., Zhang, X., and Zhou, Z. (2019a). Carbon-based substrates for highly dispersed nanoparticle and even single-atom electrocatalysts. *Small Methods* 3, 1900050.
- Chen, Z., Zhao, J., Yin, L., and Chen, Z. (2019b). B-terminated (111) polar surfaces of BP and BAs: promising metal-free electrocatalysts with large reaction regions for nitrogen fixation. *J. Mater. Chem. A* 7, 13284–13292.
- Cheng, Y., Zhao, S., Johannessen, B., Veder, J.P., Saunders, M., Rowles, M.R., Cheng, M., Liu, C., Chisholm, M.F., De Marco, R., et al. (2018). Atomically dispersed transition metals on carbon nanotubes with ultrahigh loading for selective electrochemical carbon dioxide reduction. *Adv. Mater.* 30, e1706287.
- Cui, X., Pan, Z., Zhang, L., Peng, H., and Zheng, G. (2017). Selective etching of nitrogen-doped carbon by steam for enhanced electrochemical CO₂ reduction. *Adv. Energy Mater.* 7, 1701456.
- Dai, L., Qin, Q., Wang, P., Zhao, X.J., Hu, C.Y., Liu, P.X., Qin, R.X., Chen, M., Ou, D.H., Xu, C.F., et al. (2017). Ultrastable Atomic copper nanosheets for selective electrochemical reduction of carbon dioxide. *Sci. Adv.* 3, e1701069.
- Gao, D., Arán-Ais, R.M., Jeon, H.S., and RoldanCuenya, B. (2019). Rational catalyst and electrolyte design for CO₂electroreduction towards multicarbon products. *Nat. Catal.* 2, 198–210.
- Goodpaster, J.D., Bell, A.T., and Head-Gordon, M. (2016). Identification of possible pathways for C–C bond formation during electrochemical reduction of CO₂: new theoretical insights from an improved electrochemical model. *J. Phys. Chem. Lett.* 7, 1471–1477.
- Hammer, B., and Nørskov, J.K. (2000). Theoretical surface science and catalysis—calculations and concepts. *Adv. Catal.* 45, 71–129.
- He, Z., He, K., Robertson, A.W., Kirkland, A.I., Kim, D., Ihm, J., Yoon, E., Lee, G.D., and Warner, J.H. (2014). Atomic structure and dynamics of metal dopant pairs in graphene. *Nano Lett.* 14, 3766–3772.
- He, T., Reuter, K., and Du, A. (2020). Atomically dispersed asymmetric Cu–B pair on 2D carbon nitride synergistically boosts the conversion of CO into C₂ products. *J. Mater. Chem. A* 8, 599–606.
- Huang, Y., Handoko, A.D., Hirunsit, P., and Yeo, B.S. (2017). Electrochemical reduction of CO₂ using copper single-crystal surfaces: effects of CO* coverage on the selective formation of ethylene. *ACS Catal.* 7, 1749–1756.
- Jia, C., Dastafkan, K., Ren, W., Yang, W., and Zhao, C. (2019). Carbon-based catalysts for electrochemical CO₂ reduction. *Sustain. Energy Fuels* 3, 2890–2906.
- Jiang, K., Siahrostami, S., Zheng, T., Hu, Y., Hwang, S., Stavitski, E., Peng, Y., Dynes, J., Gangisetty, M., Su, D., et al. (2018a). Isolated Ni single atoms in graphenenanosheets for high-performance CO₂ reduction. *Energy Environ. Sci.* 11, 893–903.
- Jiang, K., Sandberg, R.B., Akey, A.J., Liu, X., Bell, D.C., Nørskov, J.K., Chan, K., and Wang, H. (2018b). Metal ion cycling of Cu foil for selective C–C coupling in electrochemical CO₂ reduction. *Nat. Catal.* 1, 111–119.
- Ju, W., Bagger, A., Hao, G.P., Varela, A.S., Sinev, I., Bon, V., RoldanCuenya, B., Kaskel, S., Rossmeisl, J., and Strasser, P. (2017). Understanding activity and selectivity of metal–nitrogen-doped carbon catalysts for electrochemical reduction of CO₂. *Nat. Commun.* 8, 944.
- Kim, D., Kley, C.S., Li, Y., and Yang, P. (2017). Copper nanoparticle ensembles for selective electroreduction of CO₂ to C₂-C₃ products. *Proc. Natl. Acad. Sci. U.S.A* 114, 10560–10565.
- Kim, D., Shi, J., and Liu, Y. (2018). Substantial impact of charge on electrochemical reactions of two-dimensional materials. *J. Am. Chem. Soc.* 140, 9127–9131.

- Li, H., Wang, L., Dai, Y., Pu, Z., Lao, Z., Chen, Y., Wang, M., Zheng, X., Zhu, J., Zhang, W., et al. (2018). Synergetic interaction between Neighbouring platinum monomers in CO₂hydrogenation. *Nat. Nanotechnol.* 13, 411–417.
- Li, Y., Qian, Y., Ji, Y., Li, H., and Liu, Y. (2019). Improving selectivity of CO reduction via reducing coordination of critical intermediate. *J. Mater. Chem. A* 7, 24000–24004.
- Liang, Z.Q., Zhuang, T.T., Seifitokaldani, A., Li, J., Huang, C.W., Tan, C.S., Li, Y., De Luna, P., Dinh, C.T., Hu, Y., et al. (2018). Copper-on-Nitride enhances the stable electrosynthesis of multi-carbon products from CO₂. *Nat. Commun.* 9, 3828.
- Lin, Y.-P., Ksari, Y., Prakash, J., Giovanelli, L., Valmalette, J.-C., and Themlin, J.-M. (2014). Nitrogen-doping processes of graphene by a versatile plasma-based method. *Carbon* 73, 216–224.
- Lin, Y.C., Teng, P.Y., Yeh, C.H., Koshino, M., Chiu, P.W., and Suenaga, K. (2015). Structural and chemical dynamics of pyridinic-nitrogen defects in graphene. *Nano Lett.* 15, 7408–7413.
- Liu, J., Ma, X., Li, Y., Wang, Y., Xiao, H., and Li, J. (2018). Heterogeneous Fe₃ single-cluster catalyst for ammonia synthesis via an associative mechanism. *Nat. Commun.* 9, 1610.
- De Luna, P., Quintero-Bermudez, R., Dinh, C.T., Ross, M.B., Bushuyev, O.S., Todorović, P., Regler, T., Kelley, S.O., Yang, P., and Sargent, E.H. (2018). Catalyst electro-redeposition controls morphology and oxidation state for selective carbon dioxide reduction. *Nat. Catal.* 1, 103–110.
- Luo, G., Liu, L., Zhang, J., Li, G., Wang, B., and Zhao, J. (2013). Hole defects and nitrogen doping in graphene: implication for supercapacitor applications. *ACS Appl. Mater. Interfaces* 5, 11184–11193.
- Mahmood, J., Lee, E.K., Jung, M., Shin, D., Jeon, I.Y., Jung, S.M., Choi, H.J., Seo, J.M., Bae, S.Y., Sohn, S.D., et al. (2015). Nitrogenated holey two-dimensional structures. *Nat. Commun.* 6, 6486.
- Mistry, H., Varela, A.S., Bonifacio, C.S., Zegkinoglou, I., Sinev, I., Choi, Y.-W., Kisslinger, K., Stach, E.A., Yang, J.C., Strasser, P., et al. (2016). Highly selective plasma-activated copper catalysts for carbon dioxide reduction to ethylene. *Nat. Commun.* 7, 12123.
- Morales-Guio, C.G., Cave, E.R., Nitopi, S.A., Feaster, J.T., Wang, L., Kuhl, K.P., Jackson, A., Johnson, N.C., Abram, D.N., Hatsukade, T., et al. (2018). Improved CO₂ reduction activity towards C₂₊ alcohols on a tandem gold on copper electrocatalyst. *Nat. Catal.* 1, 764–771.
- Peng, X., Karakalos, S.G., and Mustain, W.E. (2018). Preferentially oriented Ag nanocrystals with extremely high activity and faradaic efficiency for CO₂ electrochemical reduction to CO. *ACS Appl. Mater. Interfaces* 10, 1734–1742.
- Peterson, A.A., Abild-Pedersen, F., Studt, F., Rossmeisl, J., and Nørskov, J.K. (2010). How copper catalyzes the electroreduction of carbon dioxide into hydrocarbon fuels. *Energy Environ. Sci.* 3, 1311–1315.
- Qiao, J., Liu, Y., Hong, F., and Zhang, J. (2014). A review of catalysts for the electroreduction of carbon dioxide to produce low-carbon fuels. *Chem. Soc. Rev.* 43, 631–675.
- Qu, L., Liu, Y., Baek, J.B., and Dai, L. (2010). Nitrogen-doped graphene as efficient metal-free electrocatalyst for oxygen reduction in fuel cells. *ACS Nano* 4, 1321–1326.
- Ren, W., Tan, X., Yang, W., Jia, C., Xu, S., Wang, K., Smith, S.C., and Zhao, C. (2019). Isolated diatomic Ni-Fe metal-nitrogen sites for synergistic electroreduction of CO₂. *Angew. Chem. Int. Ed.* 58, 6972–6976.
- Ren, W., and Zhao, C. (2020). Paths towards enhanced electrochemical CO₂ reduction. *Natl. Sci. Rev.* 7, 7–9.
- Robertson, A.W., Lee, G.D., He, K., Gong, C., Chen, Q., Yoon, E., Kirkland, A.I., and Warner, J.H. (2015). Atomic structure of graphenesubnanometer pores. *ACS Nano* 9, 11599–11607.
- Sarau, G., Heilmann, M., Bashouti, M., Latzel, M., Tessarek, C., and Christiansen, S. (2017). Efficient nitrogen doping of single-layer graphene accompanied by negligible defect generation for integration into hybrid semiconductor heterostructures. *ACS Appl. Mater. Interfaces* 9, 10003–10011.
- Sarfraz, S., Garcia-Esparza, A.T., Jedidi, A., Cavallo, L., and Takanabe, K. (2016). Cu-Snbimetallic catalyst for selective aqueous electroreduction of CO₂ to CO. *ACS Catal.* 6, 2842–2851.
- Sheng, Z.H., Shao, L., Chen, J.J., Bao, W.J., Wang, F.B., and Xia, X.H. (2011). Catalyst-free synthesis of nitrogen-doped graphene via thermal annealing graphite oxide with melamine and its excellent electrocatalysis. *ACS Nano* 5, 4350–4358.
- Tian, S., Fu, Q., Chen, W., Feng, Q., Chen, Z., Zhang, J., Cheong, W.C., Yu, R., Gu, L., Dong, J., et al. (2018). Carbon nitride supported Fe₂ cluster catalysts with superior performance for alkene epoxidation. *Nat. Commun.* 9, 2353.
- Wang, J., Huang, Z., Liu, W., Chang, C., Tang, H., Li, Z., Chen, W., Jia, C., Yao, T., Wei, S., et al. (2017). Design of N-coordinated dual-metal sites: a stable and active Pt-free catalyst for acidic oxygen reduction reaction. *J. Am. Chem. Soc.* 139, 17281–17284.
- Wang, Y., Han, P., Lv, X., Zhang, L., and Zheng, G. (2018a). Defect and interface engineering for aqueous electrocatalytic CO₂ reduction. *Joule* 2, 2551–2582.
- Wang, J., Gan, L.Y., Zhang, W.Y., Peng, Y.C., Yu, H., Yan, Q.Y., Xia, X.H., and Wang, X. (2018b). In situ formation of molecular Ni-Fe active sites on heteroatom-doped graphene as a heterogeneous electrocatalyst toward oxygen evolution. *Sci. Adv.* 4, eaap7970.
- Wang, Q., Ji, Y., Lei, Y., Wang, Y., Wang, Y., Li, Y., and Wang, S. (2018c). Pyridinic-N-Dominated doped defective graphene as a superior oxygen electrocatalyst for ultrahigh-energy-density Zn-air batteries. *ACS Energy Lett.* 3, 1183–1191.
- Wang, L., Chen, W., Zhang, D., Du, Y., Amal, R., Qiao, S., Wu, J., and Yin, Z. (2019a). Surface strategies for catalytic CO₂ reduction: from two-dimensional materials to nanoclusters to single atoms. *Chem. Soc. Rev.* 48, 5310–5349.
- Wang, T., Zhao, Q., Fu, Y., Lei, C., Yang, B., Li, Z., Lei, L., Wu, G., and Hou, Y. (2019b). Carbon-richnonprecious metal single atomelectrocatalysts for CO₂ reduction and hydrogen evolution. *Small Methods* 3, 1900210.
- Xu, H., Ma, L., and Jin, Z. (2018). Nitrogen-doped graphene: synthesis, characterizations and energy applications. *J. Energy Chem.* 27, 146–160.
- Xue, Y., Wu, B., Jiang, L., Guo, Y., Huang, L., Chen, J., Tan, J., Geng, D., Luo, B., Hu, W., et al. (2012). Low temperature growth of highly nitrogen-doped single crystal graphene arrays by chemical vapor deposition. *J. Am. Chem. Soc.* 134, 11060–110603.
- Yang, H.B., Hung, S.-F., Liu, S., Yuan, K., Miao, S., Zhang, L., Huang, X., Wang, H.-Y., Cai, W., Chen, R., et al. (2018). Atomically dispersed Ni(I) as the active site for electrochemical CO₂ reduction. *Nat. Energy* 3, 140–147.
- Yano, J., Morita, T., Shimano, K., Nagami, Y., and Yamasaki, S. (2007). Selective ethylene formation by pulse-mode electrochemical reduction of carbon dioxide using copper and copper-oxide electrodes. *J. Solid State Electr.* 11, 554–557.
- Ye, W., Chen, S., Lin, Y., Yang, L., Chen, S., Zheng, X., Qi, Z., Wang, C., Long, R., Chen, M., et al. (2019). Precisely tuning the number of Fe atoms in clusters on N-doped carbon toward acidic oxygen reduction reaction. *Chem* 5, 2865–2878.
- Zhang, C., Yang, S., Wu, J., Liu, M., Yazdi, S., Ren, M., Sha, J., Zhong, J., Nie, K., Jalilov, A.S., et al. (2018). Electrochemical CO₂ reduction with atomic iron-dispersed on nitrogen-doped graphene. *Adv. Energy Mater.* 8, 1703487.
- Zhao, X., and Liu, Y. (2020). Unveiling the active structure of single Nickel atom catalysis: critical roles of charge capacity and hydrogen bonding. *J. Am. Chem. Soc.* <https://doi.org/10.1021/jacs.9b13872>.
- Zhao, H., Yu, H., Quan, X., Chen, S., Zhang, Y., Zhao, H., and Wang, H. (2014). Fabrication of atomic single layer graphitic-C₃N₄ and its high performance of photocatalytic disinfection under visible light irradiation. *Appl. Catal. B Environ.* 152, 46–50.
- Zhao, J., Zhao, J., Li, F., and Chen, Z. (2018). Copper dimer supported on a C₂N layer as an efficient electrocatalyst for CO₂ reduction reaction: a computational study. *J. Phys. Chem. C* 122, 19712–19721.
- Zheng, Y., Vasileff, A., Zhou, X., Jiao, Y., Jaroniec, M., and Qiao, S.Z. (2019). Understanding the

roadmap for electrochemical reduction of CO₂ to multi-carbon oxygenates and hydrocarbons on copper-based catalysts. *J. Am. Chem. Soc.* 141, 7646–7659.

Zhou, Y., Che, F., Liu, M., Zou, C., Liang, Z., De Luna, P., Yuan, H., Li, J., Wang, Z., Xie, H., et al. (2018). Dopant-induced electron localization drives CO₂ reduction to C₂ hydrocarbons. *Nat. Chem.* 10, 974–980.

Zhou, P., Hou, X., Chao, Y., Yang, W., Zhang, W., Mu, Z., Lai, J., Lv, F., Yang, K., Liu, Y., et al. (2019). Synergetic interaction between neighboring platinum and ruthenium monomers boosts CO oxidation. *Chem. Sci.* 10, 5898–5905.

Zhu, W., Zhang, Y.J., Zhang, H., Lv, H., Li, Q., Michalsky, R., Peterson, A.A., and Sun, S. (2014). Active and selective conversion of CO₂ to CO on ultrathin Au nanowires. *J. Am. Chem. Soc.* 136, 16132–16135.

Zhu, D.D., Liu, J.L., and Qiao, S.Z. (2016). Recent advances in inorganic heterogeneous electrocatalysts for reduction of carbon dioxide. *Adv. Mater.* 28, 3423–3452.

Zhuang, T., Liang, Z., Seifitokaldani, A., Li, Y., De Luna, P., Burdyny, T., Che, F., Meng, F., Min, Y., Quintero-Bermudez, R., et al. (2018). Steering post-C–C coupling selectivity enables high efficiency electroreduction of carbon dioxide to multi-carbon alcohols. *Nat. Catal.* 1, 421–428.

Supplemental Information

**Selective C–C Coupling by Spatially
Confined Dimeric Metal Centers**

Yanyan Zhao, Si Zhou, and Jijun Zhao

Supplemental Information

Transparent Methods

Computational Methods

Our calculations were performed using the Vienna *ab initio* simulation package (VASP) based on spin-polarized density functional theory (DFT) (Kresse and Furthmüller, 1996), with the projector augmented wave (PAW) method for ion-electron interaction (Kresse and Joubert, 1999), and the generalized gradient approximation (GGA) parameterized by Perdew, Burke, and Ernzerhof (PBE) for the exchange and correction functional (Perdew et al., 1996). We used the planewave basis set with the energy cutoff of 500 eV. The Grimme's semiempirical DFT-D3 scheme of dispersion correction was adopted for a reliable description of the interactions between catalysts and reaction species (Grimme, 2010). To incorporate a metal dimer, we considered defective graphene sheets comprising holes, whose edge atoms are partially substituted by N atoms (shown in Figure 1). The supercell consists of 7×7 graphene unit cells with a lattice constant of 17.22 Å for the lateral directions, and a vacuum space of 20 Å for the perpendicular direction. We also considered two kinds of monolayer carbon nitrides with stoichiometry of C₂N and g-C₃N₄, using 2×2 unit cells with supercell dimensions of 16.64 Å and 14.26 Å, respectively. One metal dimer was placed in the hole of each model supercell structure. The Brillouin zones of all the supercells were sampled by the $2 \times 2 \times 1$ Monkhorst-Pack \mathbf{k} grids. The geometry optimization was carried out for both ionic and electronic degrees of freedom, with the convergence criteria of 10^{-4} eV and 0.02 eV/Å for energy and force, respectively. On-site charges were evaluated by the Mulliken population analysis (Mulliken, 1955) implemented in the CASTEP (Clark et al., 2005), using the planewave basis with energy cutoff of 1000 eV, the norm-conserving pseudopotentials, and the PBE functional. The climbing image nudged elastic band method was employed to search for the transition states of elementary steps and calculate the kinetic barriers (Henkelman et al., 2000).

The thermodynamic stability of a defective carbon substrate was characterized by

the formation energy per unit length defined as

$$E_{\text{form}} = (E_{\text{NxCy}} - x/2 E_{\text{N}2} - yE_{\text{C}}) / L \quad (\text{S1})$$

where E_{NxCy} is the energy of the carbon substrate comprising x numbers of N atoms and y numbers of C atoms per supercell; $E_{\text{N}2}$ and E_{C} are the energies of a N_2 gas molecule and a C atom in perfect graphene, respectively; L is the total edge length of a hole in the carbon substrate. The binding strength between the metal dimer and the carbon substrate was evaluated as

$$E_b = E_{\text{M}2@\text{NxCy}} - E_{\text{M}2} - E_{\text{NxCy}} \quad (\text{S2})$$

where $E_{\text{M}2}$ and $E_{\text{M}2@\text{NxCy}}$ are the energies of the metal dimer (M_2) in vacuum and on the carbon substrate, respectively. The thermal stability of these carbon substrate anchored metal dimers was further assessed by *ab initio* molecular dynamics (AIMD) simulations.

To characterize the interaction between reaction molecules (CO_2 and CO) and catalyst, we defined the adsorption energy as

$$\Delta E = E_{\text{total}} - E_{\text{M}2@\text{NxCy}} - E_{\text{mol}} \quad (\text{S3})$$

where E_{total} is the energy of the molecule adsorbed on the catalyst; E_{mol} is the energy of the molecule in gas phase. The Gibbs free energy of formation (ΔG) for each reaction step was calculated by including the zero-point energy and entropy (Table S3 and S4). The maximum ΔG among all the reaction steps defines the rate-determine step (RDS) and is thus denoted as ΔG_{RDS} . Then, the free energy diagrams of CO_2 reduction were obtained based on the computational hydrogen electrode model (Peterson et al., 2010).

Random simulation of N-doped carbon monolayer

To obtain the lattice structures of various N-doped carbon monolayers, we used a home-made program to generate random structures of graphene lattice with different N doping concentrations. The essential idea of the program is to produce a graphene lattice of a given size and add certain number of N dopants into it. Specifically, a lattice C atom is randomly selected to be substituted by N atom or deleted and replacing its adjacent sites with N atoms until the total number of N atoms reaches the target N content. There are three types of N atom: graphitic N, pyridinic N, and pyrrolic N. Experimentally, pyridinic N dopants in graphene are the major doping species at high

N contents (Sheng et al., 2011; Sarau et al., 2017). Thus, we mainly considered N contents from 3.6% to 15.6% (with pyridinic N and graphitic N of 3.3% ~ 15.3% and 0.3%, respectively). For each N content, we created several random lattice structures of N-doped graphene, as shown in Figure S1. In generally, the types and size of the holes increase as the nitrogen concentration increases. Particularly, 4N-V₂, 5N-V₃ and 6N-V₄ exist as the N content lower than 7.5%, and 6N-V₆ would arise as the N doping content reaches 10%.

Dynamic movie of the MD simulation on CO₂ adsorption process

As a respective, we have performed calculations to explore the dynamic process of CO₂ adsorption on Fe₂@6N-V₆ at 100 K (Supplemental Video S1) and 300 K (Supplemental Video S2) by AIMD simulations, respectively. The results show that the molecule can quickly chemisorb on the dimeric metal centers within a simulation time of 1 ps. These two movies are provided as independent files for download. Related to Figure 4.

Table S1. Adsorption energies of single and dual CO molecules (ΔE_{CO^*} , $\Delta E_{\text{CO.CO}^*}$), kinetic barriers of CO–CH and CO–CH₂ coupling, and the Gibbs free energy of formation for the rate-determine step (ΔG_{RDS}) of CH₃OH, CH₄, C₂H₄ and C₂H₅OH for the Fe₂ dimer anchored on various carbon substrates. Related to Figure 4.

Substrate	ΔE_{CO^*} (eV)	$\Delta E_{\text{CO.CO}^*}$ (eV)	Kinetic barrier (eV)		ΔG_{RDS} (eV)			
			CO–CH	CO–CH ₂	CH ₃ OH	CH ₄	C ₂ H ₄	C ₂ H ₅ OH
4N-V ₂	-2.14	-3.62	0	0.53	0.77	0.77	1.25	0.77
5N-V ₃	-2.21	-3.48	0	0.49	0.98	0.64	0.96	0.64
6N-V _{4(a)}	-1.94	-2.94	0	0.62	0.82	0.82	0.82	0.82
6N-V _{4(b)}	-2.31	-3.78	0	0.48	1.45	0.85	1.11	0.59
6N-V ₆	-2.70	-3.68	0	0	0.57	0.57	0.58	0.57
C ₂ N	-2.41	-3.56	0.23	0.38	0.94	0.94	1.76	0.70
g-C ₃ N ₄	-2.61	-4.04	0.22	0.19	1.01	1.01	1.69	1.01

Table S2. Adsorption energies of second CO₂ molecule ($\Delta E'_{\text{CO}_2*} = E_{\text{chem}} - E_{\text{phys}}$, i.e. the difference of energies between chemisorption and physisorption of second CO₂ molecule) and kinetic barriers for activating the second CO₂ molecule for the Fe₂ dimer anchored on various carbon substrates, given in the unit of eV. Related to Figure 3.

Substrate	4N-V ₂	5N-V ₃	6N-V _{4(a)}	6N-V _{4(b)}	6N-V ₆	C ₂ N	g-C ₃ N ₄
$\Delta E'_{\text{CO}_2*}$	0.12	0.52	0.44	0.20	0.42	0.68	0.22
Kinetic barrier	0.29	0.54	0.83	0.87	0.67	0.70	1.04

Table S3. Zero-point energy (ZPE) and entropic correction (*TS*) at $T = 298$ K for the molecules and intermediate species involved in CO_2 reduction on $\text{Fe}_2@\text{6N-V}_6$. The ZPE and *TS* values were obtained from the NIST-JANAF thermodynamics table for gaseous molecules (Chase, 1998), and by calculating the vibrational frequencies for reaction intermediates (Reuter and Scheffler, 2001). The Gibbs free energy of formation for each elementary step was computed as $\Delta G = \Delta E_{\text{DFT}} + \Delta \text{ZPE} - T\Delta S$ (ΔE_{DFT} is the DFT energy difference between the initial and final states). Our test calculations show that the $(\text{ZPE} - TS)$ value of a certain intermediate is very similar for the Fe_2 dimer supported by different carbon substrates, and thus the values of $\text{Fe}_2@\text{6N-V}_6$ were used throughout this work. Related to Figure 5.

Species	ZPE (eV)	<i>TS</i> (eV)	ZPE – <i>TS</i> (eV)	Species	ZPE (eV)	<i>TS</i> (eV)	ZPE – <i>TS</i> (eV)
H_2	0.29	0.41	-0.12	CO.CO^*	0.69	0.26	0.43
H_2O	0.60	0.59	0.01	CO.HCO^*	0.99	0.23	0.76
CO	0.14	0.62	-0.48	CO-CH^*	0.57	0.15	0.42
CO_2	0.31	0.67	-0.35	COH-CH^*	0.91	0.15	0.76
CH_3OH	1.39	0.79	0.60	HCO-CH^*	0.86	0.09	0.79
CH_4	1.20	0.58	0.62	CO-CH_2^*	0.88	0.17	0.71
C_2H_4	1.36	0.71	0.65	HCO-CH_2^*	1.17	0.10	1.07
$\text{C}_2\text{H}_5\text{OH}$	2.11	0.82	1.09	COH-CH_2^*	1.22	0.15	1.06
CO_2^*	0.32	0.13	0.19	HCOH-CH_2^*	1.50	0.21	1.29
COOH^*	0.65	0.19	0.46	CH-CH_2^*	1.07	0.10	0.97
CO^*	0.20	0.14	0.06	CH_2CH_2^*	1.39	0.16	1.23
$\text{CO}_2.\text{CO}_2^*$	0.59	0.29	0.30	HCOH-CH_3^*	1.81	0.22	1.59
$\text{CO}_2.\text{COOH}^*$	0.90	0.37	0.53	$\text{C}_2\text{H}_5\text{OH}^*$	2.16	0.24	1.92
COOH.COOH^*	1.23	0.30	0.93	$\text{CO.H}_2\text{COH}^*$	1.28	0.29	0.99
CO.COOH^*	0.79	0.23	0.56	$\text{CO.CH}_3\text{OH}^*$	1.60	0.31	1.29
CO.CO^*	0.39	0.11	0.28	CO.CH_2^*	0.82	0.17	0.65
CO.HCO^*	0.69	0.19	0.50	CO.CH_3^*	1.25	0.26	0.99

Table S4. Gibbs free energy of formation (ΔG) for each elementary step of CO₂ reduction on the Fe₂ dimer anchored on various carbon substrates. Related to Figure 5.

Reaction	ΔG (eV)						
	4N-V ₂	5N-V ₃	6N-V ₄	6N-V ₄	6N-V ₆	C ₂ N	g-C ₃ N ₄
			(a)	(b)			
2CO ₂ → CO ₂ .CO ₂ *	-0.31	0.09	0.74	-0.18	0.48	0.67	-0.64
CO ₂ .CO ₂ * → CO ₂ .COOH*	0.14	0.24	0.57	0.22	0.38	0.01	0.27
CO ₂ .COOH* → COOH.COAH*	0.66	0.23	0.37	0.51	-0.80	0.39	0.87
COOH.COAH* → COOH.CO*	0.07	-0.64	-0.97	-0.80	-0.39	-1.10	-1.22
COOH.CO* → CO.CO* + H ₂ O	-1.71	-0.90	-1.09	-0.96	-0.79	-0.95	-0.88
CO.CO* → CO.HCO*	0.77	0.49	0.70	0.53	0.57	0.70	1.01
CO.CO* → CO.COAH*	1.34	1.10	1.83	1.13	0.88	0.76	1.03
HCO.CO* → CO.HCOAH*	0.57	0.64	0.82	0.38	0.31	0.03	0.32
CO.HCOAH* → CO-CH* + H ₂ O	-0.27	-0.49	-1.17	-0.27	-0.28	-0.30	-0.81
CO.HCOAH* → CO.H ₂ COAH*	-1.10	-0.73	-0.95	-0.72	-0.27	0.94	0.31
CO-CH* → CO-CH ₂ *	-1.08	-0.32	0.03	-0.49	-0.49	-0.15	-0.04
CO.H ₂ COAH* → CO.CH ₂ * + H ₂ O	0.44	0.41	-0.50	0.85	0.36	-1.46	-1.22
CO.H ₂ COAH* → CO.CH ₃ OH*	-0.35	-0.24	-0.59	-0.07	-0.79	-1.89	-1.39
CO-CH ₂ * → HCO-CH ₂ *	-0.13	0.35	-0.13	-0.66	0.13	-0.52	-0.78

$\text{CO}-\text{CH}_2^* \rightarrow$							
$\text{COH}-\text{CH}_2^*$	0.28	0.14	0.32	0.28	0.28	0.46	0.10
$\text{CO. CH}_2^* \rightarrow \text{CO. CH}_3^*$	-0.94	-0.97	0.56	-1.19	-1.06	-0.21	-0.33
$\text{HCO}-\text{CH}_2^* \rightarrow$							
$\text{HCOH}-\text{CH}_2^*$	0.36	-0.18	0.15	1.06	-0.02	0.48	0.82
$\text{COH}-\text{CH}_2^* \rightarrow$							
$\text{HCOH}-\text{CH}_2^*$	-0.06	0.04	-0.30	0.12	-0.26	-0.50	-0.06
$\text{CO. CH}_3^* \rightarrow \text{CO. CH}_4^*$	-0.53	0.39	-2.04	0.65	-1.33	-1.27	-0.90
$\text{HCOH}-\text{CH}_2^* \rightarrow$							
$\text{CH}-\text{CH}_2^* + \text{H}_2\text{O}$	-0.74	-0.59	-0.23	0.22	-0.21	-0.79	-0.46
$\text{HCOH}-\text{CH}_2^* \rightarrow$							
$\text{HCOH}-\text{CH}_3^*$	0.03	0.18	-0.22	-0.03	0.01	0.02	-0.03
$\text{CH}-\text{CH}_2^* \rightarrow \text{CH}_2\text{CH}_2^*$	0.04	-0.26	-0.41	-1.04	0.14	0.05	-0.54
$\text{HCOH}-\text{CH}_2^* \rightarrow$							
$\text{C}_2\text{H}_5\text{OH}^*$	0.41	-0.55	-0.16	-0.30	0.73	-0.12	0.36
$\text{CH}_2\text{CH}_2^* \rightarrow \text{C}_2\text{H}_4$	1.25	0.96	0.23	1.11	0.58	1.11	1.69
$\text{C}_2\text{H}_5\text{OH}^* \rightarrow \text{C}_2\text{H}_5\text{OH}$	0.11	0.46	-0.04	0.59	-0.26	0.46	0.34

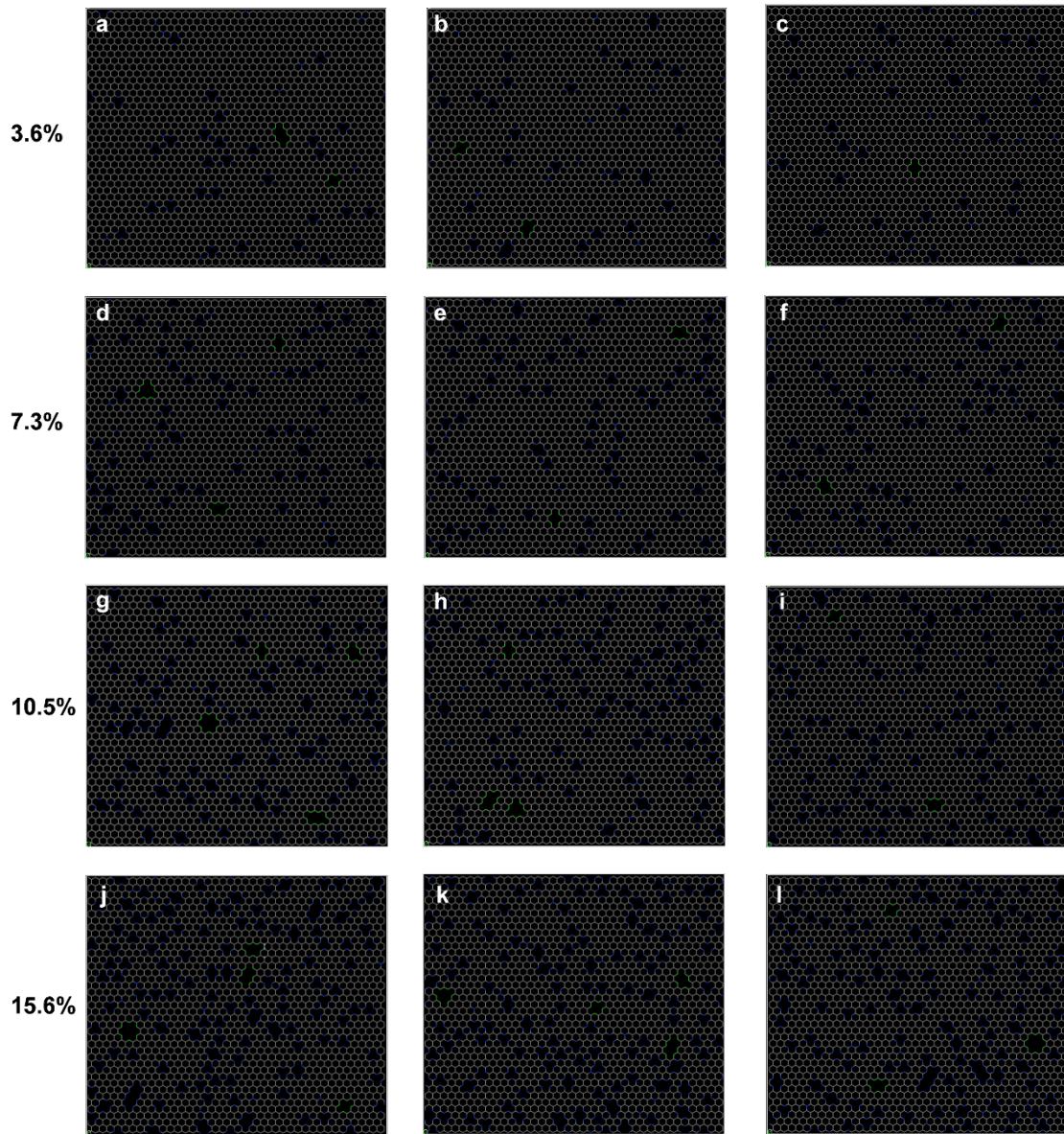


Figure S1. The N-doped carbon monolayer structures with various N content of (a, b, c) 3.6%, (d, e, f) 7.3%, (g, h, i) 10.5% and (j, k, l) 15.6%, respectively, created by our home-made program that randomly introduces pyridinic N and graphitic N into graphene lattice. The results show that 4N-V₂, 5N-V₃ and 6N-V₄ exist as the N content lower than 7.5% and 6N-V₆ configuration emerges as the N doping content reaches 10%. The C and N atoms are shown in grey and blue/green colors, respectively. The green highlights the structural models considered in this work. Related to Figure 1.

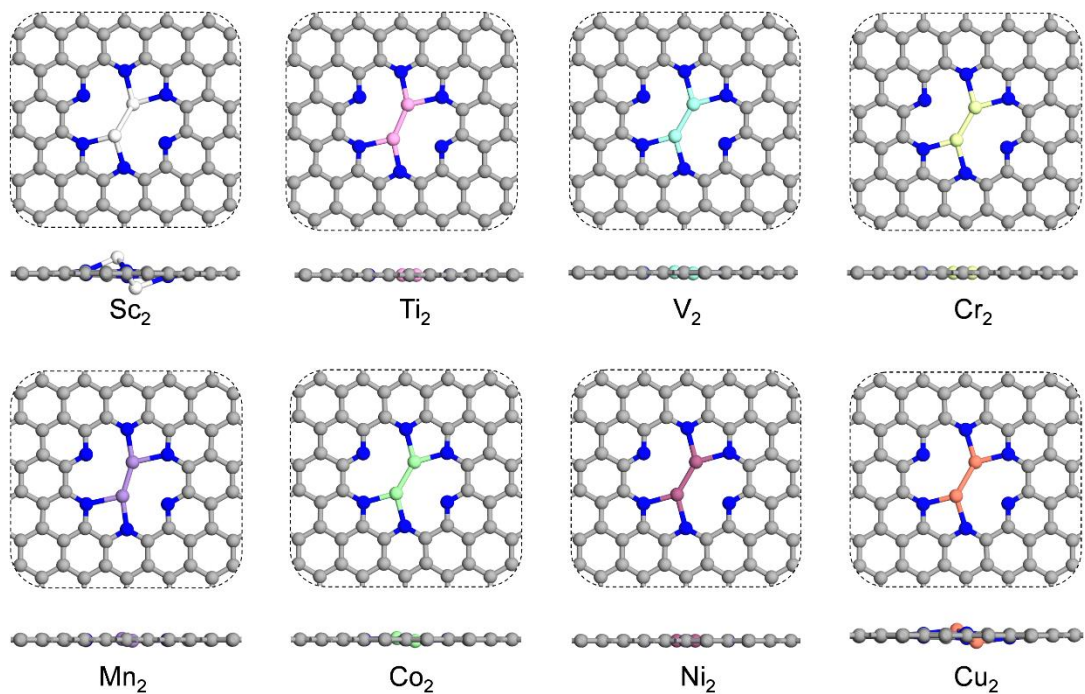


Figure S2. Atomic structures of 3d transition metal dimers anchored on the 6N-V₆ monolayer. The C and N atoms are shown in grey and blue colors, respectively. Related to Table 2.

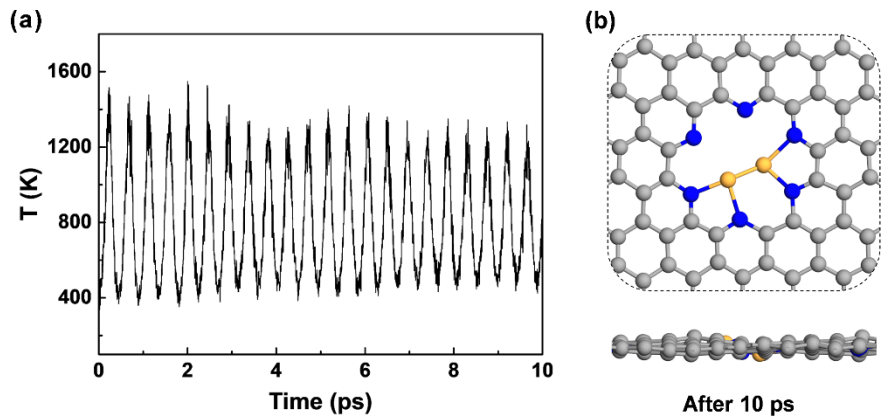


Figure S3. (a) Temperature profile and (b) snapshot atomic structure of Fe₂@6N-V₆ from *ab initio* molecular dynamics simulation at 800 K for 10 ps, which well maintains the initial equilibrium geometry with an average atomic displacement of 0.16 Å in the vertical direction. The C, N and Fe atoms are shown in grey, blue and orange colors, respectively. Related to Figure 1.

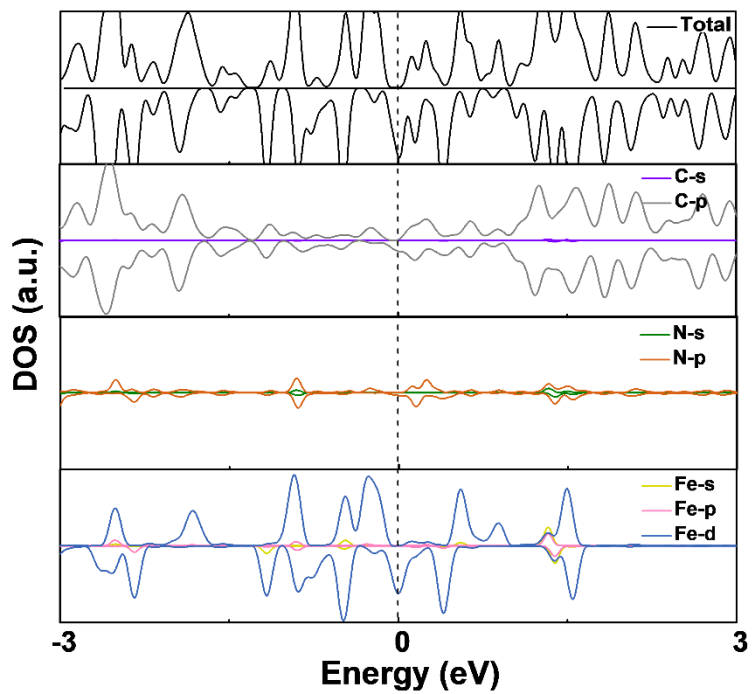


Figure S4. The projected density of states (DOS) of $\text{Fe}_2@6\text{N-V}_6$. The dashed line shows the Fermi level. Related to Figure 2.

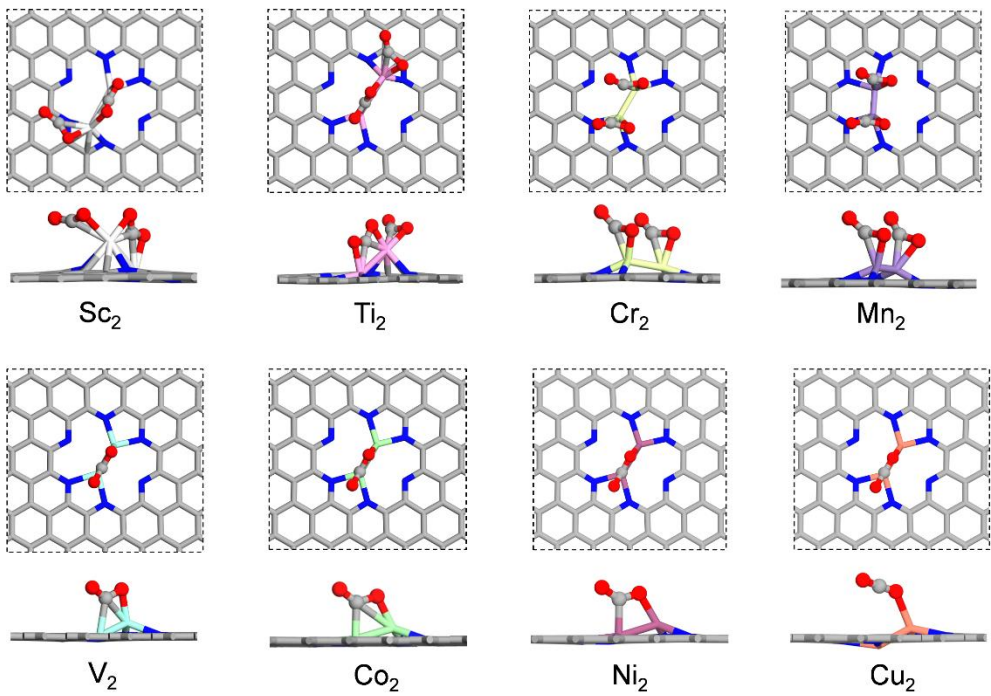


Figure S5. Atomic structures of dual or single CO₂ molecule adsorbed on 3d transition metal dimers anchored on the 6N-V₆ monolayer. The C, N and O atoms are shown in grey, blue and red colors, respectively. Related to Table 2.

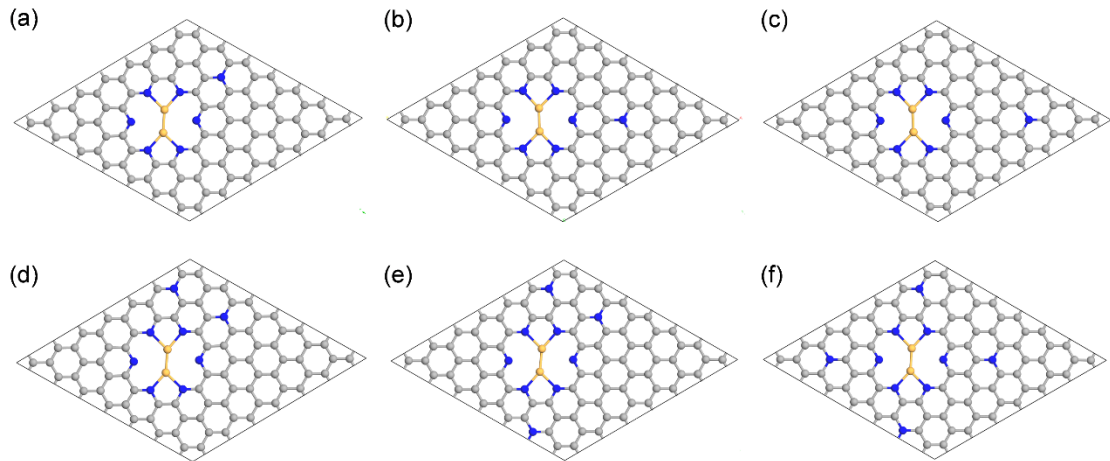


Figure S6. Model structures of $\text{Fe}_2@6\text{N-V}_6$ with presence of the graphitic N atoms near or away from the hole. For models (a), (b) and (c), we placed the graphitic N atom at different distances from the Fe_2 dimer, with $d_a < d_b < d_c$. For models (d), (e) and (f), we considered two, three and four graphitic N atoms per supercell, respectively. The C, N and Fe atoms are shown in grey, blue and orange colors, respectively. Related to Figure 1.

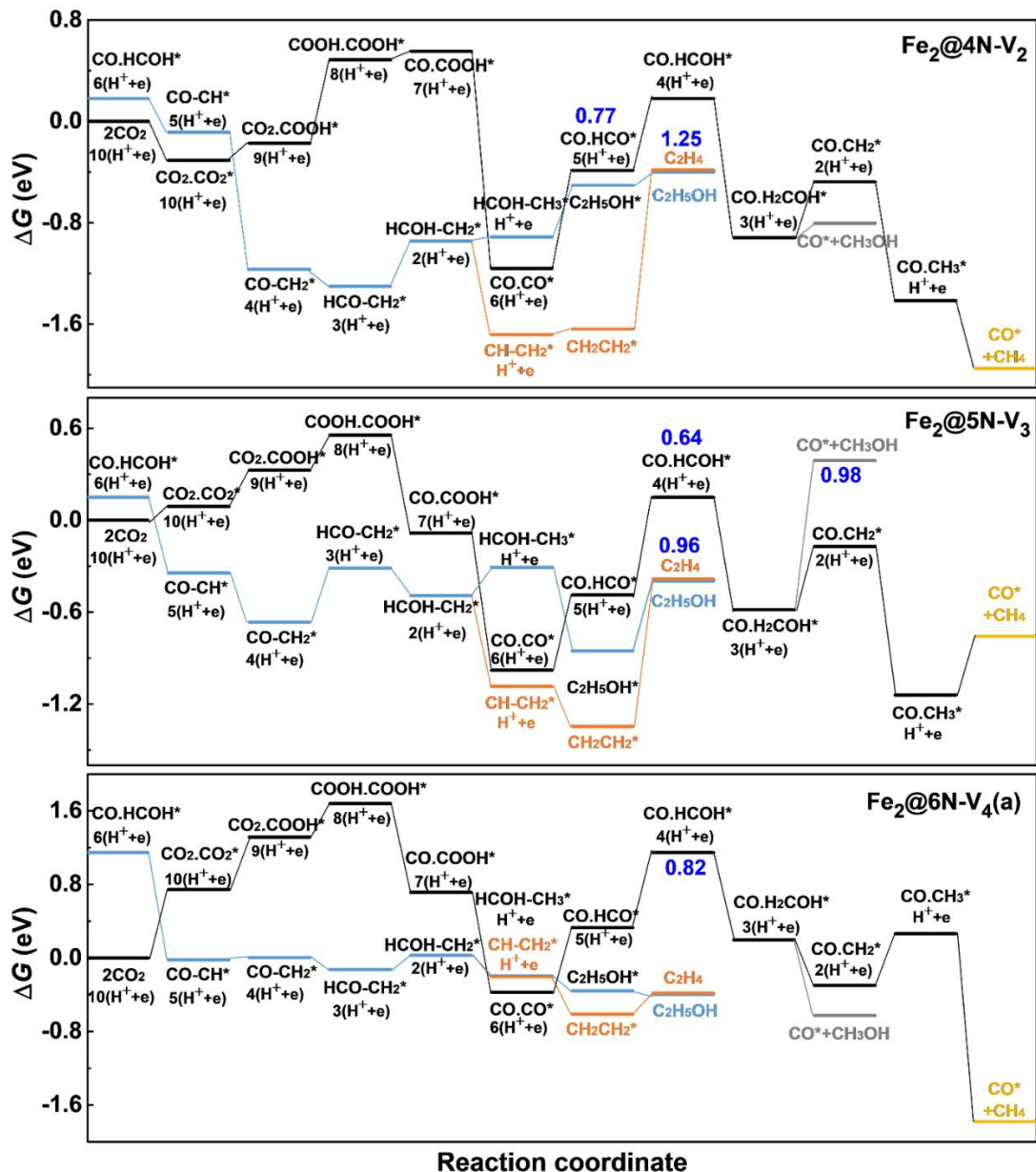


Figure S7. Free energy diagrams of CO_2 reduction to form various C_1 and C_2 products (indicated by different colors) on $\text{Fe}_2@4\text{N-V}_2$, $\text{Fe}_2@5\text{N-V}_3$ and $\text{Fe}_2@6\text{N-V}_4(a)$. The blue numbers indicate ΔG_{RDS} values for every products. Related to Figure 5.

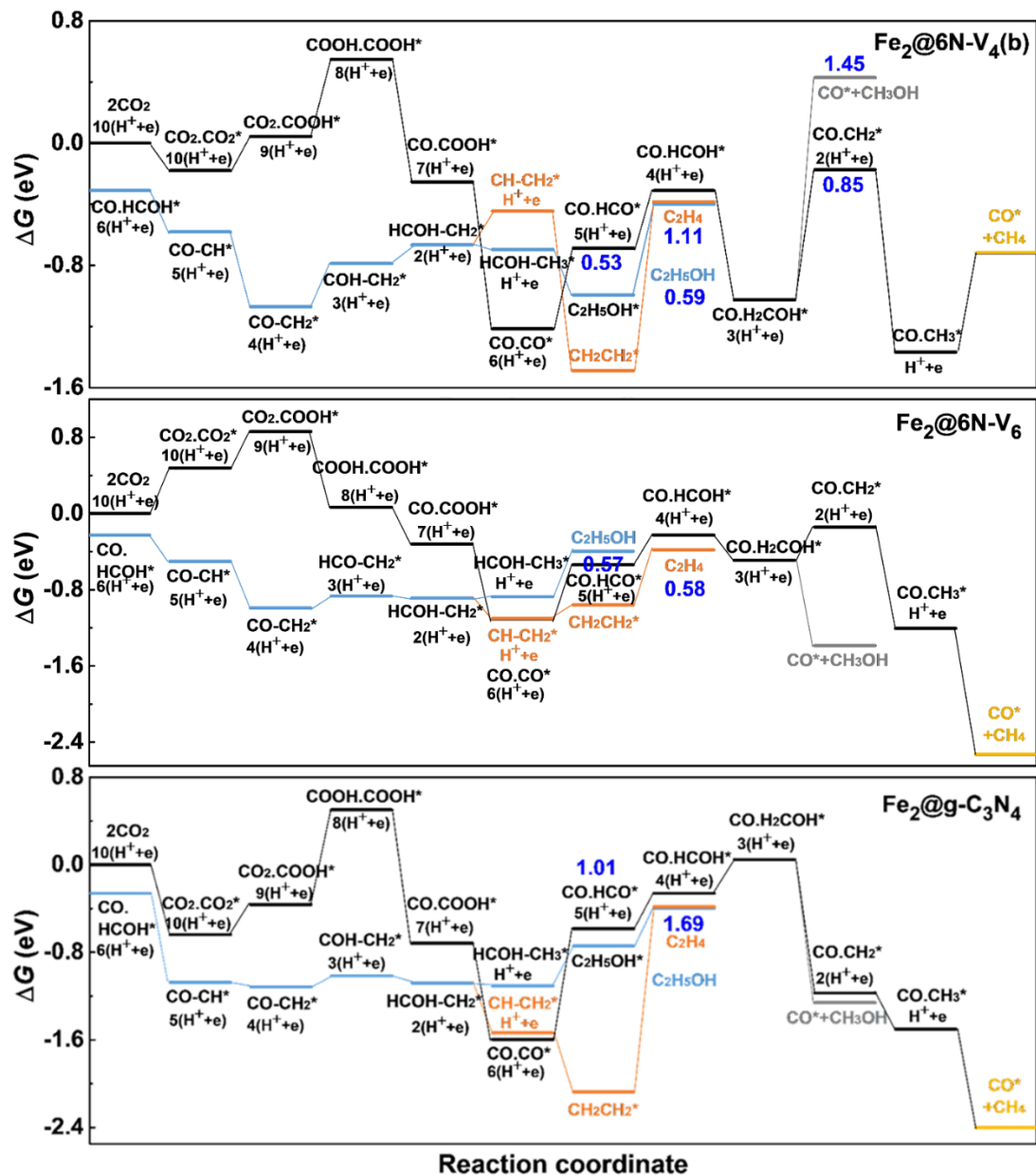


Figure S8. Free energy diagram of CO_2 reduction to form various C_1 and C_2 products (indicated by different colors) on $\text{Fe}_2@6\text{N-V}_4(\text{b})$, $\text{Fe}_2@6\text{N-V}_6$ and $\text{Fe}_2@g\text{-C}_3\text{N}_4$. The blue numbers indicate ΔG_{RDS} values for every products. Related to Figure 5.

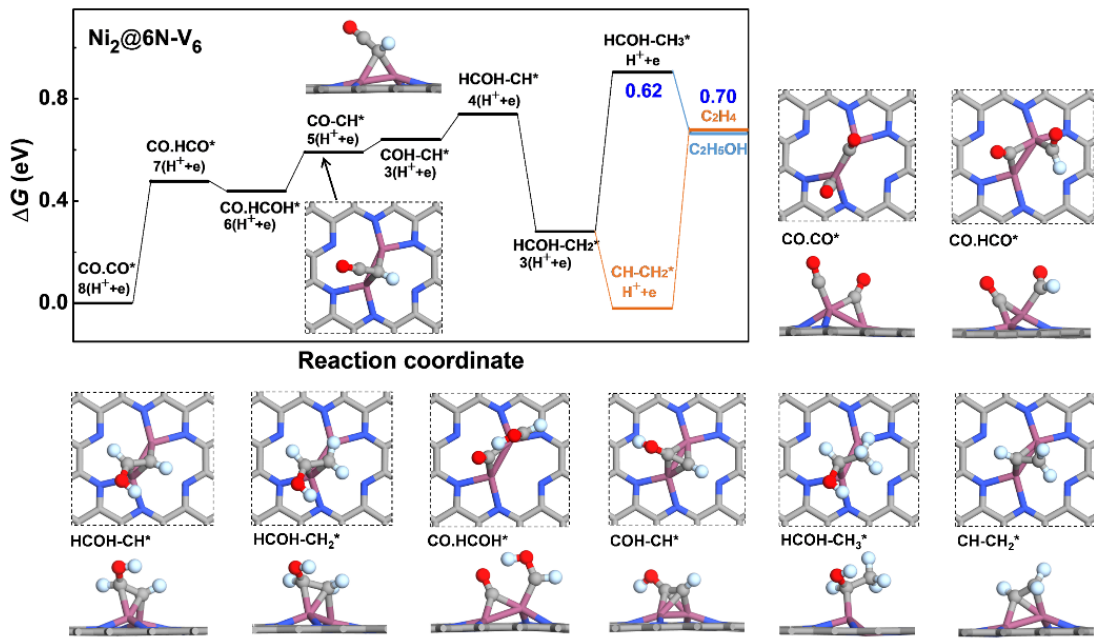


Figure S9. Free energy diagram and atomic structures of CO₂ reduction to form C₂H₄ and C₂H₅OH products (indicated by different colors) on Ni₂@6N-V₆, the free energies of rate-determining step are 0.70 and 0.62 eV for C₂H₄ and C₂H₅OH products, respectively. The blue numbers indicate ΔG_{RDS} values for every products. The H, C, N, O and Ni atoms are shown in light blue, grey, blue, red and claret colors, respectively.

Related to Figure 5.

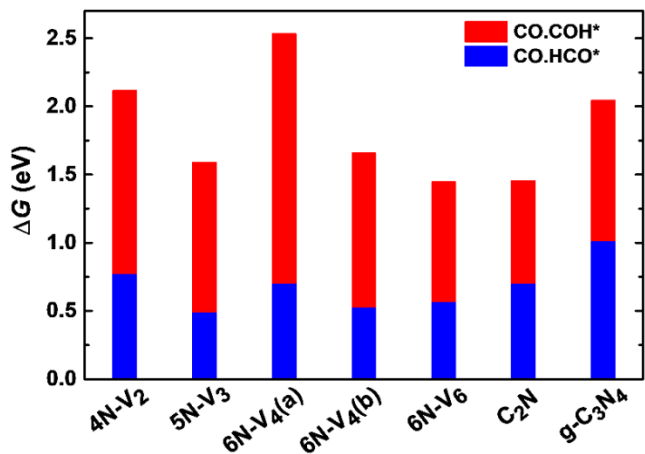


Figure S10. Gibbs free energy of formation (ΔG) for generating CO.HCO* and CO.COH* intermediates from protonation of CO.CO*. Related to Figure 4.

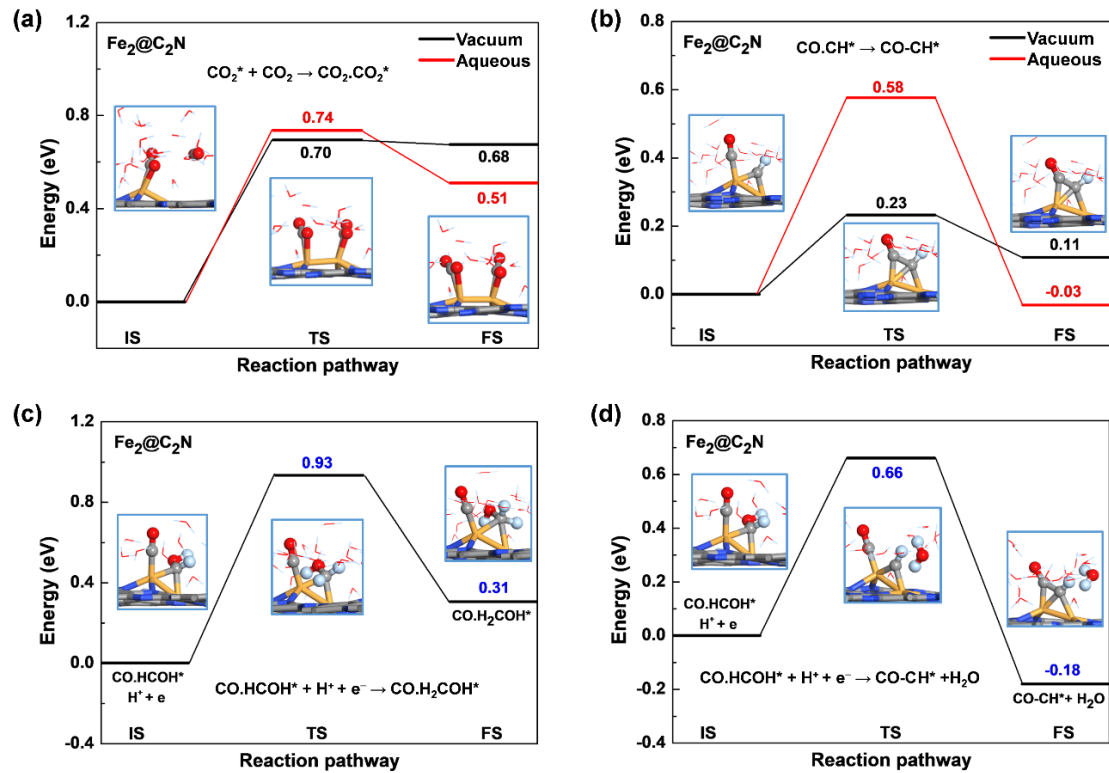


Figure S11. (a) The kinetic process of second CO_2 activation in vacuum and in the aqueous condition. (b) The $\text{CO}-\text{CH}^*$ coupling in vacuum and in the aqueous condition. Competing reactions of CO.HCOH^* to form (c) C_1 and (d) C_2 intermediates on $\text{Fe}_2@\text{C}_2\text{N}$ in water environment, respectively. The insets display the structures of initial state (IS), transition state (TS) and final state (FS). The numbers give the kinetic barriers (middle) and heat of reaction (right). The H, C, N, O and Fe atoms are shown in light blue, grey, blue, red and orange colors, respectively. Related to Table 3.

References

- Kresse, G., Furthmüller, J. (1996). Efficient Iterative Schemes for *ab initio* Total-Energy Calculations Using a Plane-Wave Basis Set. Phys. Rev. B 54, 11169-11186.
- Kresse, G., Joubert, D. (1999). From Ultrasoft Pseudopotentials to the Projector Augmented-Wave Method. Phys. Rev. B 59, 1758-1775.
- Perdew J. P., Burke, K., Ernzerhof M. (1996). Generalized Gradient Approximation Made Simple. Phys. Rev. Lett. 77, 3865-3868.
- Grimme, S., Antony, J., Ehrlich, S., Krieg, H. (2010). A Consistent and Accurate *ab initio* Parametrization of Density Functional Dispersion Correction (DFT-D) for the 94 Elements H-Pu. J. Chem. Phys. 132, 154104.
- Mulliken, R. S. (1955). Electronic Population Analysis on LCAO-MO Molecular Wave Functions. II. Overlap Populations, Bond Orders, and Covalent Bond Energies. J. Chem. Phys. 23, 1841-1846.
- Clark, S. J., Segall, M. D., Pickard, C. J., Hasnip, P. J., Probert, M. I., Refson, K., Payne, M. C. (2005). First Principles Methods Using CASTEP. Z. Kristallogr. –Cryst. Mater. 220, 567-570.
- Henkelman, G., Uberuaga, B. P., Jónsson, H. (2000). A climbing image nudged elastic band method for finding saddle points and minimum energy paths. J. Chem. Phys. 113, 9901-9904.
- Peterson, A. A., Abild-Pedersen, F., Studt, F., Rossmeisl, J., Nørskov, J. K. (2010). How Copper Catalyzes the Electroreduction of Carbon Dioxide into Hydrocarbon Fuels. Energy Environ. Sci. 3, 1311-1315.
- Sheng, Z. H., Shao, L., Chen, J. J., Bao, W. J., Wang, F. B., Xia, X. H. (2011). Catalyst-Free Synthesis of Nitrogen-Doped Graphene Via Thermal Annealing Graphite Oxide with Melamine and Its Excellent Electrocatalysis. ACS Nano 5, 4350-4358.
- Sarau, G., Heilmann, M., Bashouti, M., Latzel, M., Tessarek, C., Christiansen, S. (2017). Efficient Nitrogen Doping of Single-Layer Graphene Accompanied by Negligible Defect Generation for Integration into Hybrid Semiconductor Heterostructures. ACS Appl. Mater. Interfaces 9, 10003-10011.
- Chase, M. W. (1998). NIST-JANAF Thermochemical Tables. American Chemical Society, New York.
- Reuter, K.; Scheffler, M. (2001). Composition, Structure, and Stability of RuO₂ (110) as a Function of Oxygen Pressure. Phys. Rev. B 65, 035406.